Fluid Conductivity of Steady Two-Phase Flow in a 2D Micromodel

Analysis of a Representative 2D Percolation Model

George Hadjisotiriou (4549953)

Thesis supervisor: Prof. Rossen, W.R.

Delft, Netherlands, July 5th 2020

Delft University of Technology

Preface

This paper is the second bachelor thesis of a series and continues from work by J. Holstvoogd (2020) on the viability of two-phase flow within a 2D medium. The paper was written for AESB3400-15, an adapted version of the traditional bachelor end project (BEP) course that also includes a replacement for the by corona cancelled field development plan (FDP) of the AES curriculum. The FDP-replacement focuses on the practical application of foams within reservoir engineering by considering the technical-, socio-environmental- and economical aspects of field planning.

Those who are particularly interested in solutions for network conductivity are referred to chapter 4. In addition to this, an overview of the applications of foams within reservoir engineering is included in chapter 8.

I would also like to thank my supervisor Prof. W. Rossen for giving me his full attention to discuss my work on a weekly basis and my family for the constant support in the form of espressos.

George Hadjisotiriou
Delft
July 5th 2020

Summary

Foams are used in reservoir engineering for enhanced oil recovery, CO_2 sequestration and environmental remediation of aquifers and soils. The definition of a foam is a discontinuous dispersion of gas within a liquid that is separated by liquid lamellae. One of the main mechanisms for foam generation at steady state is considered to be Roof snap-off. Some simulations use mechanistic models for Roof snap-off based on observation from 2D microfluidic devices, such as micromodels. These micromodels are a silicon or glass wafer wherein an image of a pore space is etched on a one-to-one scale. It is first saturated with liquid and then simultaneously injected with liquid (water) and gas (nitrogen) at steady-state. The surface cross-section of the etched pore space is rectangular and has sharp corners. Under these conditions, the liquid lines the walls of the pore space and accumulates as flow conducting channels in the corners of the pore throat.

The main problem with these experiments is in their 2D nature. Two-phase flow within a 2D medium requires that the fluids paths cross and compete for pore occupancy. This virtually insures fluctuating pore occupancy and therefore puts into question the applicability of 2D mechanistic models for steady state foam generation in 3D media.

Two-phase flow in a micromodel is analyzed with a lattice percolation model in order to determine under what conditions steady two-phase flow in a micromodel can be achieved. The lattice is initially saturated with water, has a coordination number of four and a wrap-around boundary. The gas network is established with bond percolation and liquid is allowed to flow across the sample with the help of liquid bridges. These liquid bridges enable the liquid to cross gas-occupied pore throats without snap-off. The calculated attribute for the gas and liquid networks is equivalent resistance, $\Delta P/Q$. For this a new unit for hydraulic resistivity was used and is equal to the fluid viscosity divided by the pore radius to the third power, $\mathcal{H} = \mu/R^3$. The gas and liquid networks are considered as networks of pore-scale hydraulic resistances and rules from linear circuits of electrical resistances are applied directly. Solutions for the equivalent resistivity of the gas network are calculated with the node elimination method and Kirchhoff's solution for a random network of resistances. The liquid network's conductivity is calculated as the sum of path resistances in parallel and is an upper bound.

The gas and liquid conductivity of nine pre-existing 16x16 networks from Holstvoogd(2020) are reevaluated with the new methods and, in addition, twelve new samples of size 32x32 (four times larger) are evaluated.

Functionally, the model's behavior is as follows: gas conductivity is inversely proportional and liquid conductivity is proportional to the occupation thresholds. It is found that the gas conductivity is a function of tortuosity and number of parallel flow loops. Conductivity decreases with increased tortuosity and increases with number of parallel flow paths.

The ratio of liquid and gas conductivity for the twelve 32x32 models is calculated. When adjusted for gas viscosities of supercritical CO_2 and Nitrogen gas it is found that it is in the order of 10^{-3} to 10^{-4}. Therefore, it has been determined that it is practically impossible to achieve steady two-phase flow without fluctuating pore occupancy.

Table of Contents

1. Introduction

Foams are commonly used in enhanced oil recovery (EOR) to improve poor sweep efficiency of the reservoir from early gas breakthrough. During breakthrough gas establishes a preferential flow path to the production well, thus largely bypassing portions of the reservoir and decreasing the efficiency of oil recovery. To prevent this, foams are introduced into the reservoir for gas mobility control and plugging of highly permeable thief zones. Reducing the mobility of the gas delays breakthrough and increases dispersion thus improving contact with the reservoir volume and increasing oil recovery. During plugging, thief zones which are potential zones for preferential flow paths are plugged in order to divert flow into other zones of the reservoir. Other applications of foams include CO_2 sequestration and environmental remediation of aquifers and soils.

A recent point of study is the viability of experimental observations of Roof snap-off in 2D mediums to reflect on foam generation within 3D media. In particular, the possibility of steady state two-phase flow within a 2D medium is questioned. Many mechanistic models and simulations for foam generation in 3D are based on conclusions made in 2D-micromodel experiments. Hence, it is of great importance that flow in 2D is thoroughly understood. It is known from percolation theory that in an isotropic media only one phase can establish a flowing network at any time. This virtually guarantees fluctuating pore occupancy and calls into question Roof snap-off's importance as a foam generation mechanism at steady-state. Yet, the possibility of steady two-phase flow within a 2D micromodel is entertained by the possibility of liquid bridging the gas along the top and bottom of the throat to eventually establish its own liquid network (Rossen, 2003; Kovscek et al., 2007; Rossen, 2008).

The purpose of this paper is to estimate the gas and liquid conductivity of a micromodel at steady flow conditions with liquid bridging. To this extent, bond percolation is used to produce random gas networks within a representative homogeneous 2D lattice. Liquid flow paths are then established within the residual water-saturated pores. Estimations for the gas and liquid conductivity are first made on the pore-scale before being applied to the networks themselves.

The paper is structured as follows:

- Chapter two introduces the percolation model.
- Chapter three makes an estimation for the resistivity of gas within a rectangular pore throat.
- Chapter four describes the solution methods for the equivalent conductivity of the gas network.
- Chapters five makes an estimate for the liquid resistivities on a pore-scale.
- Chapter six discusses the conductivity of the liquid network.
- Chapter seven contains the results of the gas and liquid conductivities of the models.
- Chapter eight discusses the application of foams within EOR, carbon capture and storage (CCS) and environmental remediation from an engineering perspective.

1.1. Mechanisms for foam generation

Rossen (1996) defines foams as 'a dispersion of gas in liquid such that the liquid phase is interconnected and at least some gas flow paths are blocked by lamellae'. Modeling foam is done as a multiphase problem with liquid (wetting phase) lining the walls of the pore volume and gas (non-wetting phase) in the middle. There are three main mechanisms for foam generation illustrated in figure 1.1. These are leave-behind, snap-off and lamella division (Rossen, 1996; Almajid & Kovscek, 2019).

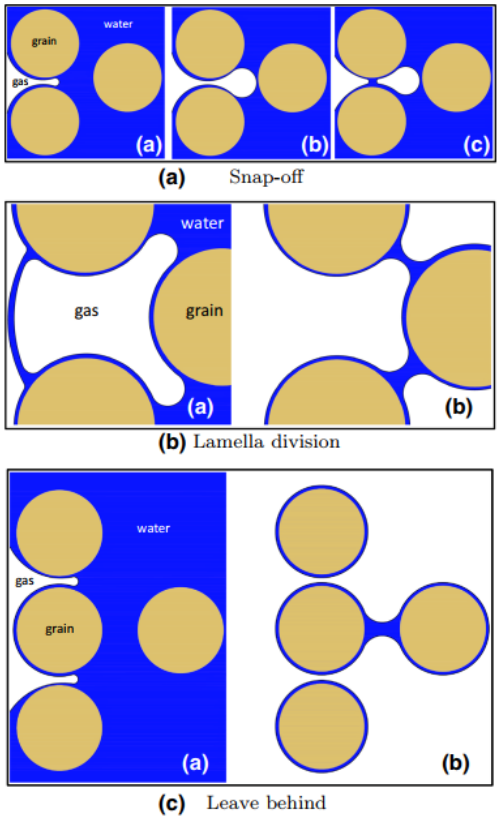

Figure 1.1: Illustration of the three different foam generation mechanisms from (Almajid & Kovscek, 2019)

During leave-behind, lamellae are created as gas invades the medium and displaces liquid from two pores next to each other. During the establishment of the gas path lamellae are created in between the rock grains parallel to the direction of gas flow.

Snap-off for foam generation occurs in pore throats when water accumulates to the extent that the water crosses the throat and gas flow is blocked (Rossen, 1996; Kovscek et al. 2007). To start, gas enters the pore throat when the capillary pressure rises to the capillary entry pressure, P_{ce}, at which point gas flows through the throat. After this snap-off occurs when the capillary pressure decreases to the snap-off capillary pressure. Subsequently, the newly formed liquid lens or lamella is moved by invading gas out of the throat and into the connecting pore body. For foam generation to occur this must happen repeatedly allowing for the formation of a discontinuous gas phase within the medium. The snap-off pressure of the throat depends on the pore geometry and is described as a fraction of the capillary entry pressure, P_{ce}. For a square throat the capillary entry pressure is half the capillary entry pressure. Rossen (2003) gives and overview of the snap-off pressures for different pore geometries.

Lamellae division occurs during lamellae mobilization when a lamella enters a pore body with several pore throats. In this case the lamella will either break or split into new lamellae that continue into each pore throat of the body.

1.2. Micromodel observations of Roof snap-off

Experimentally, Roof snap-off has been observed in constricted tube experiments and microfluidic devices. Roof snap-off refers to snap-off that depends on the ratio of the bore body to pore throat diameters (Rossen, 2008). In a microfluidic experiment an image of a pore space is etched into a

glass or silicon wafer to create a synthetic porous medium through which fluid is injected, this is the micromodel. Kovscek et al. (2007) conducted a micro visual analysis of flow in a silicon micromodel with simultaneous injection of water and N_2(gas) and found that snap-off occurs repeatedly at germination sites. From their observations they state that snap-off is the "dominant mechanism" for foam generation within homogenous media.

What follows is details of their device. The micromodels pore space has a rectangular geometry with sharp unrounded corners and a depth of $25\mu m$ (see figure 1.2(a)). Additionally, the pore throats width ranges from $12\mu m$ to $25\mu m$. The model is initially saturated with water before the simultaneous injection of liquid and gas at steady flow rates through distribution channels (see figure 1.2(b)). Experiments are conducted at a fractional gas flow rate (gas rate/total injection rate) of above 0,9 (Kovscek et al., 2007).

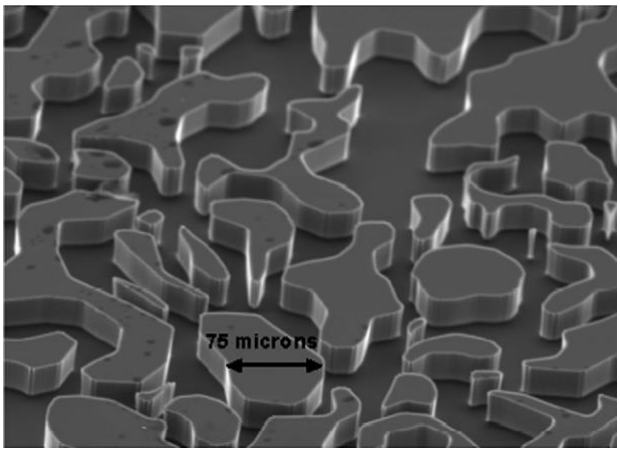

Figure 1.2(a): SEM image of the etched pore network. From the picture the square/rectangular pore geometry can be seen. (Kovscek et al., 2007)

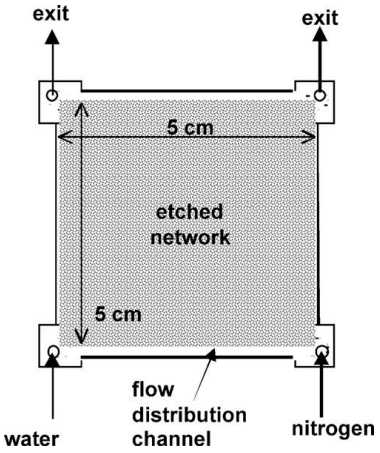

Figure 1.2(b): schematic representation of the micromodel. (Kovscek et al., 2007)

An issue with this experiment is whether two-dimensional flow experiments like this one can actually reflect on steady state foam generation within a homogenous porous medium in 3D. The problem is that maintaining steady state in a 2D network is exceedingly difficult because the gas and liquid flow paths cross and compete for pore occupancy whereas this problem is not present in 3D pore networks. Additionally, conducting foam generation experiments in 2D also suppresses lamella division as the coordination number of the pores is smaller (Rossen, 2008). From these facts, Rossen (2008) states that "micromodels are problematic for the study of snap-off" since they virtually guarantee snap-off by themselves. Kovscek et al. (2007) on the other hand state that micromodels can represent flow in sandstone reservoir media because flow in 2D is significantly more restricting than in 3D. In addition to this they also states that "Pore occupancy does not fluctuate during steady state flow" in the micromodel.

The contents of this paper reflect on the possibility of two-phase flow in 2D medium. It continues from the work of Holstvoogd (2020) who made a 2D percolation model for flow through a 2D medium. The produced networks had a size of 16x16 pores and a rough estimate was made for their gas and liquid conductivity. Here, new networks are made with a size of 32x32 in addition to those of Holstvoogd (2020) and their exact gas conductivity is calculated by applying solutions for resistors in a random network. A new unit for resistivity is defined in eq. 1.1 as the fluid viscosity (μ) divided by the radius of the throat (R) to the third power. The liquid conductivity of the lattice is estimated by considering flow paths as a series of pore-scale resistances and adding up the paths.

$$\mathcal{H} = \frac{\mu}{R^3} \quad (1.1)$$

2. A two-dimensional percolation model

One way to achieve the required steady state conditions in a two-dimensional flow regime is to establish liquid bridges across gas-occupied pore throats that are both stable (no snap-off) and conduct enough gas through the throat. A lattice percolation model is utilized here to represent a two dimensional medium (micromodel). Disorder is introduced within the 2D lattice by bond percolation and the final result is a lattice with pores and throats filled either by water or gas.

The two-dimensional lattice consists of bonds that represent pore throats and the intersection of the bonds are the pore bodies. Connectivity is determined by the coordination number of the pore bodies and in this case is equal to 4, signifying that each pore has four connecting pore throats. Additionally, the lattice is initially saturated with water such that pores unoccupied during invasion are saturated with water and are automatically part of the liquid network.

In bond percolation the gas connectivity of the network is established by randomly assigning a probability to every bond. Bonds with a value above the percolation threshold enable flow and are assigned a conductivity value of 1 while bonds below the percolation threshold block flow and have a conductivity of 0. It is assumed that bonds with a value of 1 conduct gas while bonds with a conductivity of 0 simply remain filled with water (Hunt & Sahimi, 2017). Hunt & Sahimi (2017) give an overview of the percolation thresholds for some common 2D and 3D networks. The percolation threshold of an infinite lattice is the largest fraction of conducting bonds required to establish a sample spanning cluster (SSC). The SSC is a cluster of gas-occupied pores and throats that connect from one edge to the other and thus enable network wide flow. In a finite network the fraction of conducting bonds required to establish the SSC is referred to as the occupation threshold instead of the percolation threshold. The occupation thresholds value is random but centers around 0,5. The larger the networks the more the occupation threshold approaches the percolation threshold.

An example of the lattice used in this paper is given in figure 2.1 below. From the SSC the gas backbone is identified as the portion of the gas network that contributes to flow across the lattice/medium. The lattice has a wrap-around boundary where gas flowing out of one boundary continues to flow on the other side of the lattice. Furthermore, there are portions of the lattice that do not contribute to flow across the lattice. These are the dangling ends and the isolated clusters. Dangling ends lead to dead ends and do not contribute to lattice connectivity. Isolated clusters are clusters that do not connect to the edge of the lattice and therefore cannot possibly contain any gas. These are deleted from the lattice upon completion of the SSC, and thus remain occupied by water.

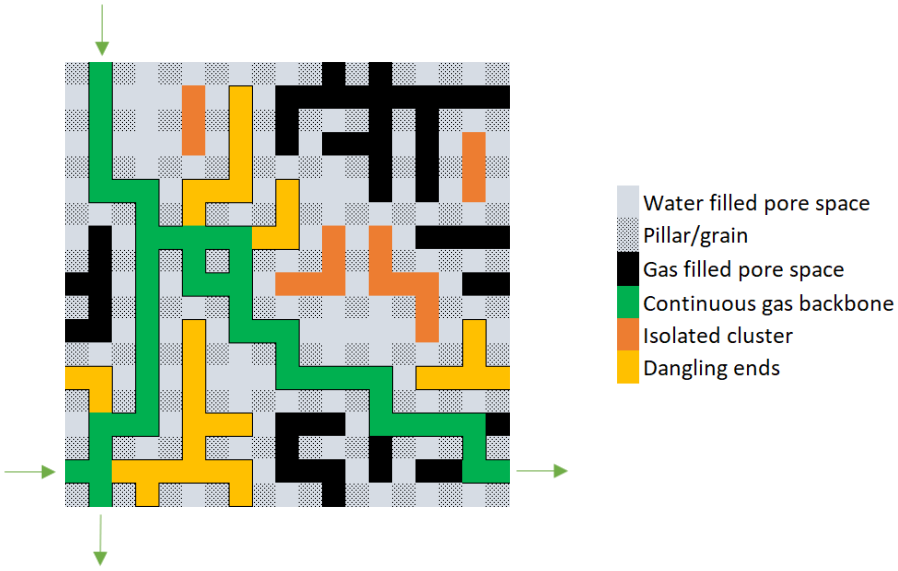

Figure 2.1: an example of a lattice and its constitutive components. After bond percolation the gas network is established. Gas flows through the gas backbone from one edge to the other in the vertical and horizontal directions.

It is important to note that the pillars are represented in figure 2.1 as rectangular but they are actuality assumed to be cylindrical. The cross-section of the throat however is rectangular.

3. Gas conductivity through one pore throat

The gas conductivity is calculated by estimating the conductivity of the individual bonds as pore throats with a rectangular cross section as illustrated in figure 3.1 and then applying solutions for a random network of resistors to the gas backbone. Throats are assumed to have a fixed width (W) of two times the pillar (grains) radius (R). The resistivity, $\Delta \mathrm{P}/\mathrm{Q}$, to flow in the pore throat is calculated in the newly defined units of $\mathcal{H} = \mu/\mathrm{R}^3$ so that the solution can be computed for a specific pore throat size, radius $\mathrm{R}[m]$, and phase viscosity $\mu\ [\mathrm{Pa} \cdot \mathrm{s}]$.

The individual throats or bonds of the gas backbone are rectangular and occupied by liquid and gas at steady state. The system is water-wet and the liquid remains in the corners around the solid pillars as channels for liquid flow, while the non-wetting phase, gas, occupies the middle of the throat. The liquid-gas interface has a circular arc in the cross-section of the throat.

The gas conductivity is determined for a variety of pore throats with a fixed width, W, of $2\mathrm{R}$ and different heights, b. No readily available flow formula exists for the gas cross-section described in figure 3.1. Therefore, the surface through which the gas flows is divided in two such that the formula for gas flow through a tube can be applied to flow through surface G_2 and the formula for flow in a slit can be used for flow through surface G_1.

$$\mathrm{Q}_{\mathrm{gas}} = \mathrm{Q}_{\mathrm{G1}} + \mathrm{Q}_{\mathrm{G2}} = \mathrm{Q}_{\mathrm{slit}} + \mathrm{Q}_{\mathrm{tube}} = \frac{2}{3}\frac{\mathrm{B}^3 \mathrm{W}}{\mu_{\mathrm{g}}}\frac{\mathrm{dP}}{\mathrm{L}} + \frac{\pi \mathrm{R}^4}{8\mu_{\mathrm{g}}}\frac{\mathrm{dP}}{\mathrm{L}}; (3.1)$$

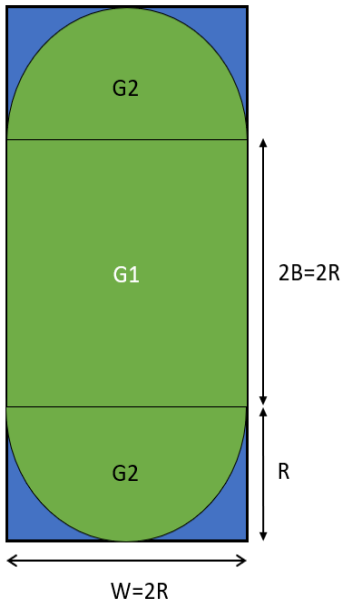

Figure 3.1: Rectangular pore throat with water in the corners and gas in the middle.

This calculation assumes that the shear stress at the boundary of G_1 and G_2 is zero. Furthermore, the liquid-gas interface is a no-slip boundary $(\mathrm{v} = 0)$ because the viscosity of gas relative to water is nearly zero. Hence, the formula for fluid flow in a tube can be used for G_2.

The formula for $\mathrm{Q}_{\mathrm{gas}}$ is converted to resistivity, $\mathrm{R}_{\mathrm{bond}}$, and written as a function of the pore throats aspect ratio b/a. Both the length (L) and the width $(\mathrm{W} = \mathrm{a})$ are assumed to be equal to the diameter of the pillar, $2\mathrm{R}$. A maximum bond resistance of approximately $5\mathcal{H}$ is found for a square pore and for $\mathrm{b}/\mathrm{a} \to \infty$ the bond resistance approaches 0 (see figure 3.2). Additionally, it is found that the resistance, R^*, for a pore throat with aspect ratio $\mathrm{b}/\mathrm{a} = 2{,}2$ is equal to 1.

$$\mathrm{R}_{\mathrm{bond}} = \frac{\mathrm{dP}}{\mathrm{Q}_{\mathrm{gas}}}\left(\frac{\mathrm{b}}{\mathrm{a}}\right) = 2\left[\frac{\pi}{8} + \frac{4}{3}\left(\frac{\mathrm{b}}{\mathrm{a}} - 1\right)\right]^{-1} \mathcal{H} \text{ for } \frac{\mathrm{b}}{\mathrm{a}} \in [1, \infty]; (3.2)$$

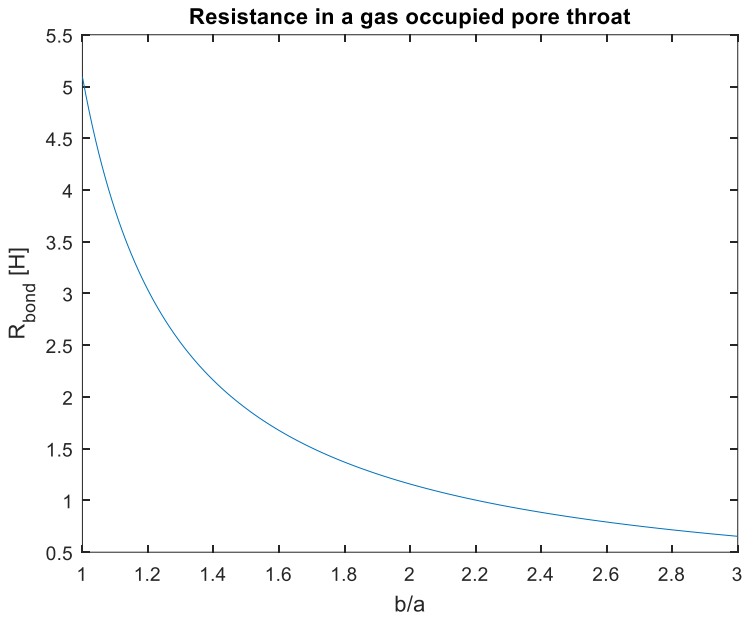

Figure 3.2: Resistance for gas flow in the pore throat is inversely proportional to the height of the pore throat.

The mobility of nitrogen gas ($\mu_{H_2O}/\mu_{N_2} = 50$) within the pore is computed for different aspect ratios and pore sizes in figure 3.3. The gas-mobility, $\lambda\ [m^3/(Pa \cdot s)]$, is multiplied by the pressure gradient, $\nabla P[Pa]$, to calculate the flow rate, $Q[m^3/s]$ through a pore throat.

$$\lambda = \frac{R^3}{2\mu}\left[\frac{\pi}{8} + \frac{4}{3}\left(\frac{b}{a} - 1\right)\right]; (3.3)$$

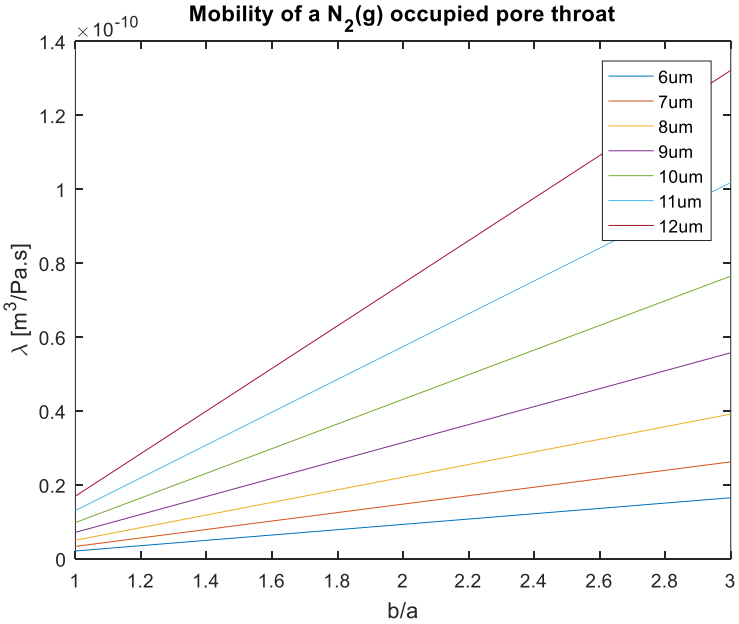

Figure 3.3: Mobility of nitrogen gas in the pore throat

4. Solutions for gas network conductivity

Solutions for the equivalent resistance of a network of resistors are used to solve for network wide gas conductivity. Bonds in the network are considered as pore throats or electrical resistors and voltage differences represent pressure differences in a fluid network.

It is possible to solve for the equivalent conductance of the network by utilizing the transformations for conductances in parallel (eq. 4.1), series (eq. 4.1) and the delta-T transformation (eq. 4.3-5) (Frank & Lobb, 1988). By continuously applying these transformations to the bonds within the network, the network will eventually be reduced to a single bond with the equivalent resistance of the network. For bonds in parallel the conductance is equal to the sum of the bonds.

Parallel: $G_{eq} = \sum G_i; (4.1)$

For bonds in series it is equal to the sum of the inverses of the individual conductance's.

Series: $\frac{1}{G_{eq}} = \sum \frac{1}{G_i}; (4.2)$

The delta-T transformation is performed by converting the previously unsolvable T-junction to the more manageable delta circuit where parallel and series rules can be applied correctly (see figure 4.1) (Frank & Lobb, 1988).

Delta-T transformation for $T \rightarrow \Delta$:

$$G_A = \frac{G_2 G_3}{G_1 + G_2 + G_3}; (4.3)$$

$$G_B = \frac{G_1 G_3}{G_1 + G_2 + G_3}; (4.4)$$

$$G_C = \frac{G_1 G_2}{G_1 + G_2 + G_3}; (4.5)$$

From figure x it can be seen that G_C and G_B are now in series and their equivalent resistance is in parallel with G_A.

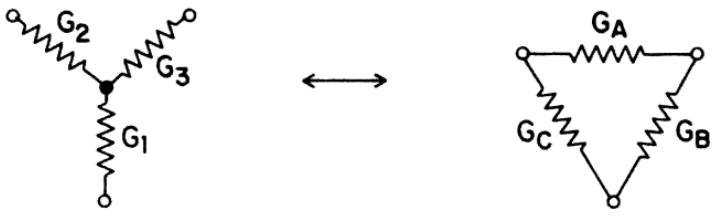

Figure 4.1: Schematic representation of the delta-T transformation.
Adapted from Frank & Lobb, 1988.

Although a solution can be obtained manually it is preferable to let a program do the work. To that extent two methods are implemented in MATLAB. These two solutions are Kirchhoff's solution and the node elimination solution. When utilized, both correctly return the same answer. However, there are some differences in usability that do make a difference.

Kirchhoff's solution is computationally much more efficient and thus quicker but node elimination allows for non-uniform bond descriptions where Kirchhoff's solution does not. A program that can accept non-uniform bond descriptions is better suited for modelling of heterogenous media.

The solution is computed from the graph of the gas backbone. Therefore, it must first be separated from the SSC in Excel and then imported into MATLAB. Doing this is necessary for Kirchhoff's solution but is not strictly necessary when using the node elimination method. However, its is recommended because it will dramatically increase the computational efficiency of the node elimination method.

After separating the gas backbone, a highly adapted version of Holstvoogds (2020) script for bond percolation is implemented as a function to convert the array of values into an edge list. This script can be found in appendix B3. The edge list is a vector containing the end nodes of each edge and is used in MATLAB's *graph* function to create a network graph (see figure 4.2). The wrap-around boundary is satisfied by adding an edge that connects both sides.

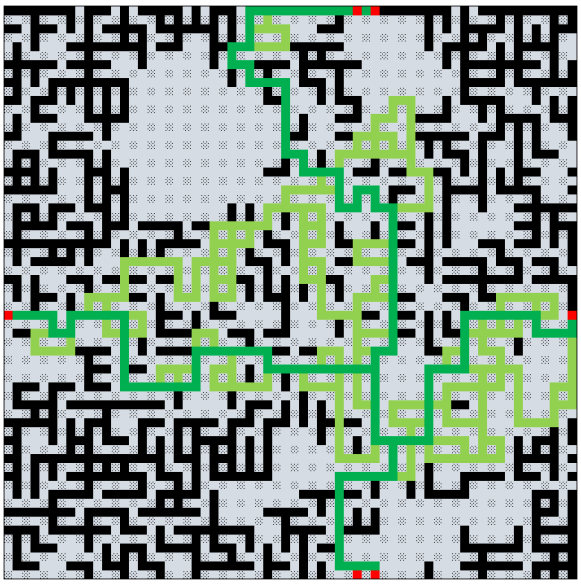

Figure 4.2(a): Network 4 (p=0,51), Excel array of the entire network. The gas backbone is colored in green and separated from the rest.

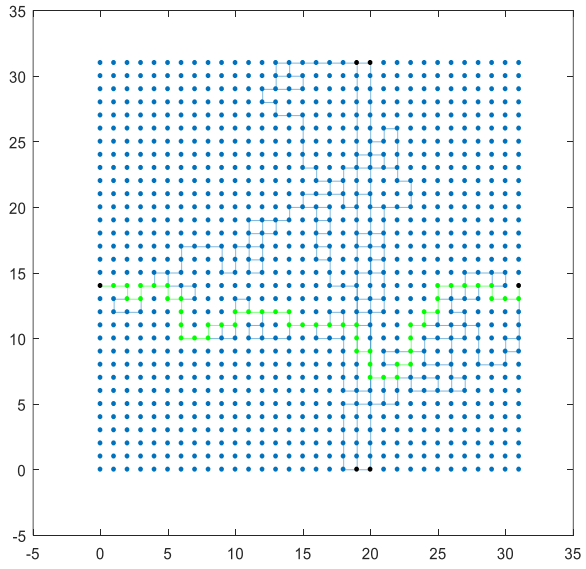

Figure 4.2(b): The gas backbone is plotted as a network graph in MATLAB. The top and bottom boundary are connected (black nodes) to satisfy the wrap-around boundary.

Both solution methods can measure the equivalent resistivity between any two nodes of the network. However, in order to calculate the equivalent conductivity across a sample with several external nodes, terminal nodes (X and Y) are added to the boundaries to which the external nodes connect. External nodes are defined here as nodes on the lattice boundaries where fluid crosses the boundary. In the example of figure 4.2(b) they are marked in black. The equivalent resistance is then calculated between these two terminal nodes, X and Y (Fogelholm, 1980). Doing this does however does assume that these external boundaries are at the same pressure. In a physical sense the terminal nodes are the distribution channels of the micromodel presented by Kovscek et al. (2008). This interpretation may be counterintuitive considering that a channel physically resembles a pore throat but with a width of $500\mu\mathrm{m}$ its dimensions are 20 to 40 times that of the throats within the network.

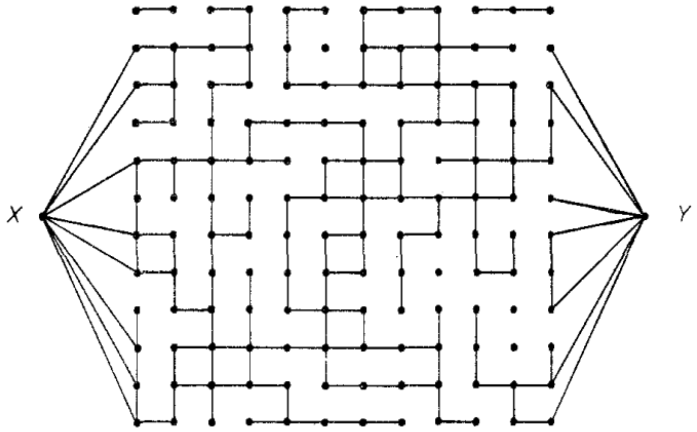

Figure 4.3: Percolation sample with terminal nodes X and Y (Fogelholm, 1980)

One of the assumptions for the lattice model is that the radii of the pore throats are uniform and therefore the bond conductivity is also uniform. The network conductivity, $\mathrm{C}_{\mathrm{eq}}^{\mathrm{b/a}}$, for a specific pore throat with $\mathrm{C}_{\mathrm{bond}}^{\mathrm{b/a}}$ is calculated from the solution for network conductivity with $\mathrm{C}_{\mathrm{bond}}^{*} = 1\mathcal{H}^{-1}$ in equation 4.6.

$$\mathrm{C}_{\mathrm{eq}}^{\mathrm{b/a}} = \mathrm{C}_{\mathrm{eq}}^{*} \times \mathrm{C}_{\mathrm{bond}}^{\mathrm{b/a}} = \mathrm{C}_{\mathrm{eq}}^{*} \times \frac{1}{\mathrm{R}_{\mathrm{bond}}^{\mathrm{b/a}}}; (4.6)$$

The same can be done for the equivalent resistance of the network with specific bond resistance $R_{bond}^{b/a}$ in equation 4.7.

$$\mathrm{R}_{\mathrm{eq}}^{\mathrm{b/a}} = \mathrm{R}_{\mathrm{eq}}^{*} \times \mathrm{R}_{\mathrm{bond}}^{\mathrm{b/a}}; (4.7)$$

Furthermore, it is worth pointing out that the bond resistance is equal to the equivalent resistance of a fully occupied lattice. When the network is fully occupied all the pore throats of the networks are in series and in parallel with each other and therefore $R_{eq} = R_{bond}$. For proof:

32 pore throats in series per flow path: $\mathrm{R_{series}} = \sum \mathrm{R_{bond}} = 32\mathrm{R_{bond}}$

And 32 flow paths in parallel: $\mathrm{R_{eq}} = \frac{1}{32 \times \frac{1}{32\mathrm{R_{bond}}}} = \mathrm{R_{bond}}$

4.1. Kirchhoff's solution

To implement Kirchhoff's solution the graph is made up of uniform bonds of $1\mathcal{H}$ randomly distributed in a square grid with nodes numbered by $\mathrm{i} = 1,2, \dots, \mathrm{N}$. The two-point resistance (eq. 4.8) is the resistance between the two connected nodes k and l, $\mathrm{R_{kl}}$. Nodes k and l are defined as terminal nodes of the network and are connected to an outside current source I of $1\mathrm{A}$. The current is injected in node k and retrieved from the ground l so eq.4.8 reduces to $\mathrm{V_k}$.

$$\mathrm{R_{kl}} = \frac{\mathrm{V_k} - \mathrm{V_l}}{\mathrm{I}} = \mathrm{V_k}; \ (4.8)$$

Kirchhoff's Current Law states that the net current at node $\mathrm{I_i}$ is equal to sum of currents flowing into node i. In equation 4.9 the current of a bond is represented as the product of bond conductance $\mathrm{x_{ij}}$ and the voltage difference $(\mathrm{V_i} - \mathrm{V_j})$.

$$\mathrm{I_i} = \sum \mathrm{x_{ij}} \left(\mathrm{V_i} - \mathrm{V_j}\right); \ (4.9)$$

Kirchhoff's equations are written in matrix form (eq. 4.10) where $\vec{\mathrm{V}}$ is the voltage vector with the unknown voltages and $\vec{\mathrm{I}}$ is the current vector containing the external currents (Knudsen & Fazekas, 2006). Here current is inserted into the terminal nodes because they are nodes that are connected to only one resistor instead of two (Rommes & Schilders, 2010).

$$\vec{\mathrm{I}} = \mathcal{L}_{\mathrm{G}} \, \vec{\mathrm{V}}; \ (4.10)$$

The conductance matrix $\mathcal{L}_{\mathrm{G}}$ contains the degree (number of connected edges) of each node on the diagonal and the incidence of each node as the row and column elements (Wu, 1982).

$$\mathcal{L}_{\mathrm{G}} = \begin{cases} -\sum_{\mathrm{j}=1}^{\mathrm{N}} \mathrm{x_{ij}}, & \text{for } \mathrm{i} = \mathrm{j} \\ -\mathrm{x_{ij}}, & \text{for } \mathrm{i} \neq \mathrm{j} \end{cases}$$

In the case that the bond conductance is defined as $1\mathcal{H}^{-1}$ then the conductance matrix is the same as the Laplacian of the network graph and is found by subtracting the adjacency matrix from the degree matrix. Additionally, the conductance matrix can also be calculated from the incidence matrix of the graph: $\mathcal{L}_G = I_G I_G^T$. Important properties of the conductance matrix are that it is sparse, symmetric (Redner, 2012) and that the sum of each row/column is zero (Wu, 1982).

The solution for the two-point resistance (eq. 4.11) is found by computing the determinant of the conductance matrix with rows and columns k and l removed for $|\mathcal{L}_G\backslash(k,l|k,l)|$ and row and column l removed for $|\mathcal{L}_G\backslash(l|l)|$ (Wu, 1982; Serra, 2005).

$$\mathrm{R_{kl}} = \frac{1}{\mathrm{x_{kl}}} = \frac{|\mathcal{L}_\mathrm{G}(\mathrm{k},\mathrm{l}|\mathrm{k},\mathrm{l})|}{|\mathcal{L}_\mathrm{G}(\mathrm{l}|\mathrm{l})|} \quad (4.11)$$

This solution follows from Kirchhoff's solution (eq. 4.12) for the effective conductance between nodes k and l (eq. XX) and the principal-minor matrix-tree theorem (Serra, 2005). In Kirchhoff's solution for conductance between nodes k and l is equal to the number of spanning trees $T(G)$ of graph G divided by the number of spanning trees of subgraph $\mathrm{G}\backslash\mathrm{k},\mathrm{l}$.

$$\mathrm{x_{kl}} = \frac{\mathrm{T(G)}}{\mathrm{T(G\backslash k,l)}} \quad (4.12)$$

The principal-minors matrix-tree theorem states that number of spanning trees can be determined with these relations: $|\mathcal{L}_G\backslash(k,l|k,l)| = T(G\backslash k,l)$ and $|\mathcal{L}_G\backslash(l|l)| = T(G)$.

4.2. Node elimination

In node elimination the star-mesh transform is implemented to systematically transform the network into an equivalent one without changing its conductivity (Derrida et al., 1984; Fogelholm, 1980). To do this the generalized form of the previously mentioned delta-T transformation, the star-mesh transformation, is utilized. With this formula nodes and their connecting edges are systematically removed but the conductivity remains the same since adjacent nodes are connected either with a new edge or one with a higher value. When node $\mathrm{X_0}$ and connecting edges $\mathrm{x_1}, \mathrm{x_2}, \ldots, \mathrm{x_n}$ are eliminated new edges are added between adjacent nodes k and l according to equation 4.13 below (Fogelholm, 1980; Knudsen & Fazekas, 2006).

$$\Delta\mathrm{x_{kl}} = \frac{\mathrm{x_{k0}x_{l0}}}{\sum_{\mathrm{i=1}}\mathrm{x_{i0}}}; \quad (4.13)$$

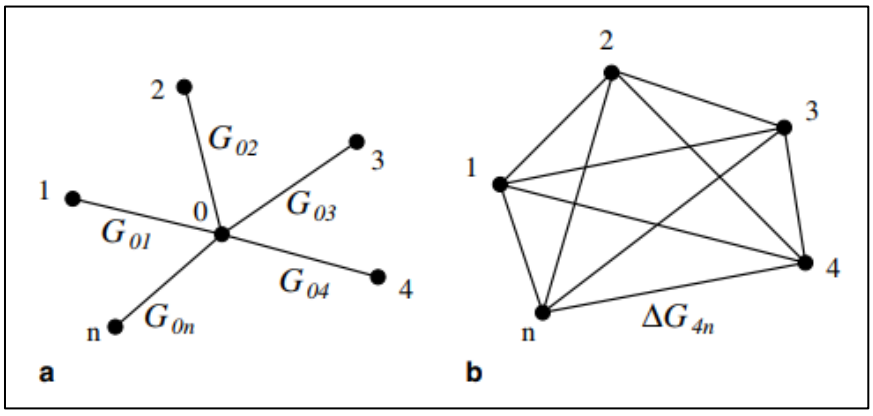

Figure 4.4: State of the network before (a) and after (b) removing node 0 (source: Knudsen & Fazekas, 2006)

The process for node removal is iterative and the number of nodes will grow exponentially. Consequently, it is computationally very intensive and especially so for networks below the percolation threshold (Fogelholm, 1980). Therefore, it is worth considering the order in which the nodes are removed. In this script nodes are eliminated according to their degree. The most common degree is found and nodes with that degree are then eliminated from the network so that with every iteration the number of connected nodes is reduced by as much as possible. Typically, for this lattice configuration this means that it starts with nodes of degree two and three. An alternative to this approach is to first calculate the consequence of removing each node and then eliminate the node that reduces the amount of bonds by the most.

5. Liquid conductivity on a pore-scale

For liquid to flow at a steady-state through a two-dimensional lattice it is required to cross or travel along the gas-occupied throat. The liquid that accumulates in the pores corner as channels allow the liquid to flow along the side of the pillar or eventually across the roof or floor of the throat. The pore throat is considered at steady state and at the verge of liquid snap-off so that the amount of liquid present within is generously estimated. Holstvoogd (2020) illustrates in figure xxx three movements of liquid that pose a significant resistance for the liquid flow paths. The first, R_1, is a 90-degree turn along the pillar. The second, R_2, also travels along the pillar but continues straight and the last one the liquid bridge, R_b, crosses the pore throat.

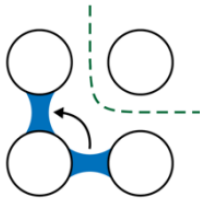

Figure 5.1(a): R1 liquid (blue) flows between and along pillars adjacent to gas in a 90-degree turn. (Holstvoogd, 2020)

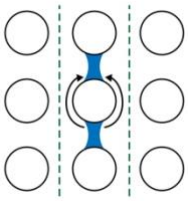

Figure 5.1(b): R3 liquid (blue) flows between and along pillars adjacent to gas in a straight path. (Holstvoogd, 2020)

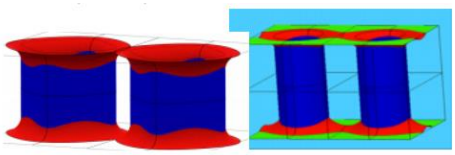

Figure 5.1(c): Liquid channels of double channel morphology in red (Cox, 2019)

5.1. Resistance to liquid flow in the corners

To estimate the resistance of the liquid movements Ransohoff and Radke's (1988) solution for "laminar flow of a wetting liquid along the corners of a predominantly gas-occupied noncircular pore" is used. Ransohoff and Radke (1988) assume that the liquid flow in the pore throat is entirely contained within the corners as illustrated by figure 3.1 and 5.2. They assume that the liquid lining film on the walls of grains is of molecular thickness and inconducive to flow. Furthermore, they tabulate a dimensionless resistance factor β as a function of the half angle (α), degree of roundness (R_0), wettability (ψ) and surface viscosity (η). The flow rate for four channels of liquid (eq. 5.1) is purposely estimated generously. Beta is minimized for a square pore $(\alpha = \pi/4)$ by assuming that the surface viscosity, wettability and degree of roundness (sharp corner) are all zero. Therefore, it is determined that the appropriate β for a square pore with sharp corners is $93{,}93$.

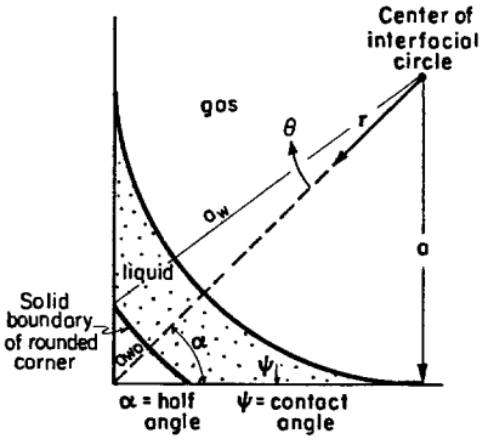

Figure 5.2: Flow within the corner of the pore throat. Degree of roundness; $R\_o = (a_{wo} - a_w)/(a_{wo} - a)$ and a= radius of curvature (Ransohoff and Radke, 1988)

The liquid flow rate for the channels is given by equation 5.1 (Rossen, 2003) where R, the pillar radius, is the same as the primary radius of curvature a from figure 5.2.

$$Q = \frac{R^4(4-\pi)}{\mu\beta}\frac{\Delta P}{\Delta z};\ (5.1)$$

From equation 5.1 the flow resistance for four channels is determined with equation 5.2. as equal to $219\mathcal{H}$.

$$R = \frac{dP}{Q} = \frac{2\beta}{4-\pi}\frac{\mu}{R^3} = 219\mathcal{H};(5.2)$$

All the channels within the throat are in parallel with each other so for a single channel the resistance is calculated as $875\mathcal{H}$ in equation 5.3.

$$R_s = 4 \times 219\mathcal{H} = 875\mathcal{H};(5.3)$$

The resistance for the liquid movements (eq. 5.4 and eq 5.5) is proportional to the distance and inversely proportional to the number of channels. For R_1 (see Fig. 5.1(a)) the length along the pillar is estimated as $(\pi/4)\ R$ and there are 2 channels. The resistance R_1 is equal to $171\mathcal{H}$.

$$R_1 = 875\mathcal{H} \times \frac{1}{2} \times \frac{\frac{\pi}{4}R}{2R} = 171\mathcal{H};\ (5.4)$$

For R_2 (Fig. 5.1(b)) the length along the pillar is estimated as $(2\pi/3)R$ and there are 4 channels for flow. The resistance R_2 is equal to $229\mathcal{H}$.

$$R_2 = 875\mathcal{H} \times \frac{1}{4} \times \frac{\frac{2\pi}{3}R}{2R} = 229\mathcal{H};\ (5.5)$$

5.2. Resistance to liquid flow in the liquid bridge

Under some circumstances, liquid flows across the gas-occupied pore along the roof and floor of as a liquid bridge (see Fig. 5.1(c)). The thickness of the liquid is estimated to be about $0.15R$ and the shear stress in the gas at the liquid-gas boundary is zero. In the formula for flow in a slit the shear stress in the middle, at $x = 0$, is zero. Therefore, the flow in the two liquid bridges (eq. 5.6) can be estimated with the slit formula with a height of $0.30R$ or $B = (0.30/2)\ R$.

$$Q = \frac{2}{3}\frac{\Delta P B^3 W}{\mu_w L};\ (5.6)$$

From equation 5.6 the resistance of the liquid bridge is computed as $444\mathcal{H}$ (see eq. 5.7).

$$R_b(B = 0.15R) = \frac{3\mu}{2(0.15)^3R^3} \approx 444\mathcal{H};\ (5.7)$$

6. Liquid conductivity on a network scale

The conductivity of the liquid network is estimated by manually identifying the different flow paths and adding up their respective conductivities.

Elements within the paths are in series and are added up accordingly (eq. 5.8). It is important to note that the conductivity of the liquid occupied pore throats is not included within the path conductivity because their resistance is so low relative to that of R_1, R_2 and R_b. The resistance of a liquid occupied pore is calculated with the formula for a slit (eq. 5.9) and has a maximum value of $R = 1{,}5\mathcal{H}$ with $B = R$ (a square throat) and $W = L = 2R$.

$$R_{path} = n_1 R_1 + n_2 R_2 + n_b R_b; \ (5.8)$$

$$Q = \frac{2}{3}\frac{\Delta P B^3 W}{\mu L} \rightarrow R = 1{,}5\mathcal{H}; \ (5.9)$$

The conductivity of the liquid networks is taken to be the sum of the path's conductivities (eq. 5.10). Liquid flow paths are added to the total conductivity until their value becomes so low that they contribute very little to the network's conductivity or until no unique paths can be identified. By adding up the conductivities of the liquid paths it is assumed the solution for liquid network conductivity is an upper bound.

$$C_{network} = \sum C_{path}; \ (5.10)$$

7. Results

The gas conductivity is determined with a pore geometry of aspect ratio b/a=2.2 (C^*) and corresponding conductivity of $1\mathcal{H}$ unless mentioned otherwise. Two data sets are available. The first consists of nine 12x12 networks (appendix B1) from Holstvoogd (2020) and the second consists of twelve 32x32 networks (appendix B2). The gas conductivity is calculated for both data sets but the liquid conductivity is only estimated for the 32x32 data set so the ratio of the liquid and gas conductivities is only available for the 32x32 dataset.

7.1. Gas network conductivity

Vertical versus horizontal network conductivity

Several flow paths exist in each direction therefore necessitating the need for the addition of two fictitious terminal nodes between which the equivalent conductivity is determined. External nodes of the lattice are either connected to the opposing side of the sample or to the terminal nodes depending on the direction in which the conductivity is determined.

External nodes on the boundaries parallel to the flow direction are connected to the opposite side in accordance to the wrap-around condition and external nodes on the boundaries perpendicular to the flow direction are connected to the terminal nodes. The conductivity of the gas backbone is determined for both the vertical and horizontal directions whenever possible for nine 16x16, networks from Holstvoogd (2020) the results of which can be seen in figure 7.1.

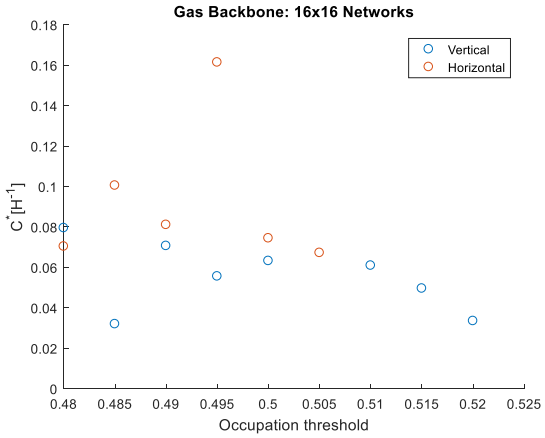

Figure 7.1: Gas conductivity per direction versus the occupation threshold; cases from appendix B1. 16x16 Networks

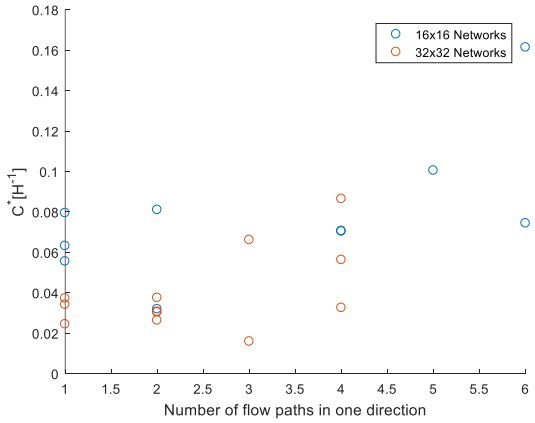

Figure 7.2: Gas conductivity versus the number of flow paths; cases from appendix B1. 16x16 Networks and appendix B2. 32x32 Networks

The data presented in figure 7.1 indicates that the difference in vertical and horizontal conductivity can either be substantial or minimal. This is a consequence of the randomness of the percolation lattice.

Number of flow paths

The gas conductivity and corresponding number of flow paths is determined for both datasets. The data is presented in figure 7.2 and it can be seen that the conductivity is independent of the number of flow paths per direction or in other words the number of external nodes connected per terminal. This is because at random there may be a bottleneck where all flow paths must pass which can drastically affect conductivity. Examples in figure 7.3(a) and 7.3(b) illustrate how a lattice with many flow paths will have a significantly lowered conductivity due to a constriction through which all fluid must flow.

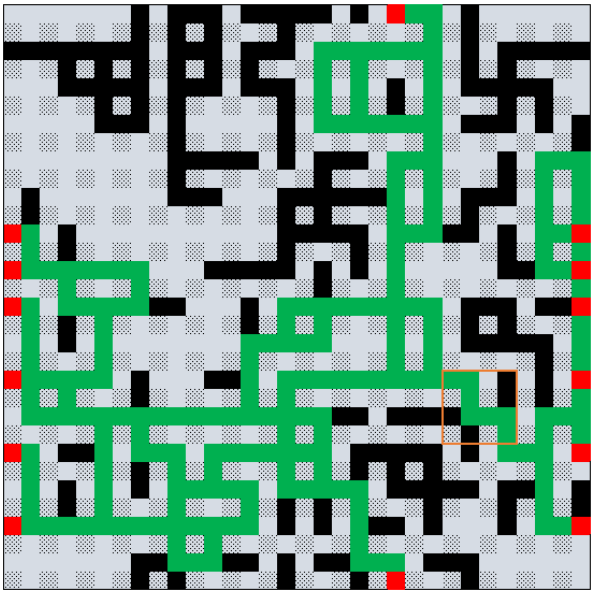

Figure 7.3(a): 16x16 network with occupation threshold p=0,50 and 6 flow paths in the horizontal direction constricted by a bottleneck (orange square) has a conductivity of $\mathrm{C_{WE}} = 0.07436\mathcal{H}^{-1}$.

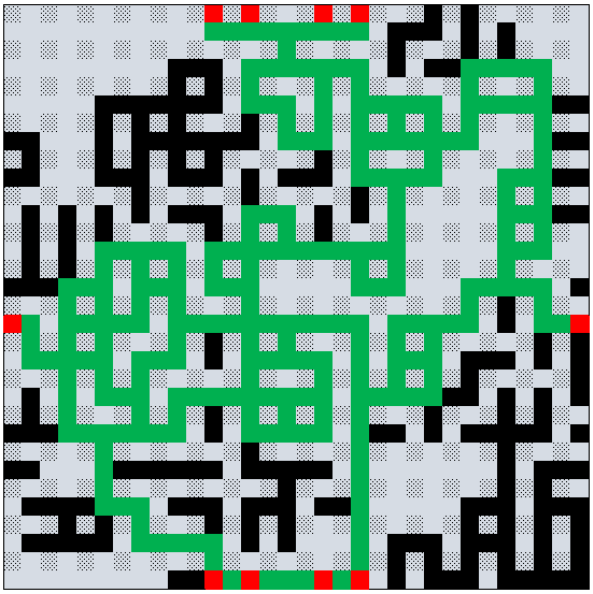

Figure 7.3(b): 16x16 network with occupation threshold p=0,48 and only 1 flow path in the horizontal direction has a conductivity of $\mathrm{C_{WE}} = 0.07942\mathcal{H}^{-1}$ *but no significant bottleneck*

Gas backbone versus minor gas path

The effect of excluding all or a number of parallel flow paths from the backbone is analyzed by considering the conductivity of the minor gas path and the “primary” gas backbone as determined by Holstvoogd (2020). The minor gas path is the shortest path between the terminal nodes and does not contain any parallel bonds whatsoever. An example can be found in figure 4.2(b) highlighted in neon green. The primary gas backbone is identified by Holstvoogd (2020) and includes a minor portion of the parallel bonds. The difference per flow direction is analyzed for nine 16x16, networks.

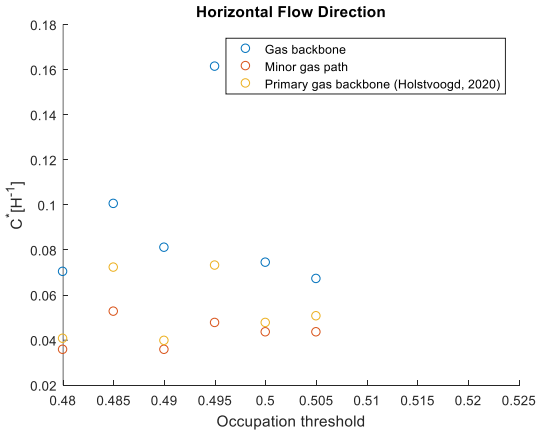

Figure 7.4(a): Conductivity of the gas backbone (exact), minor gas path and primary gas backbone in the horizontal direction; cases from appendix B1. 16x16 Networks

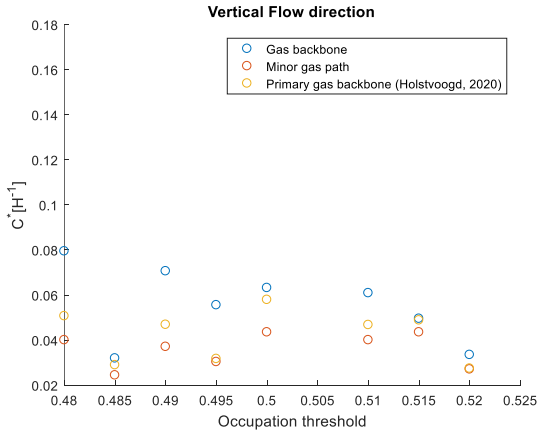

Figure 7.4(b): Conductivity of gas backbone (exact), minor gas path and primary gas backbone in the vertical direction; cases from appendix B1. 16x16 Networks

The data in figures 7.4(a) and 7.4(b) shows that the network conductivity is universally underestimated when using the minor gas path and the primary gas backbone as a quick estimator. This is because parallel flow paths contribute positively to the conductivity of a network and are left out in these off-the-cuff estimations. The difference with the gas backbone (see Fig. 7.5) is smaller at higher occupation thresholds and therefore the minor gas path and primary backbone estimations become more accurate for higher occupation thresholds.

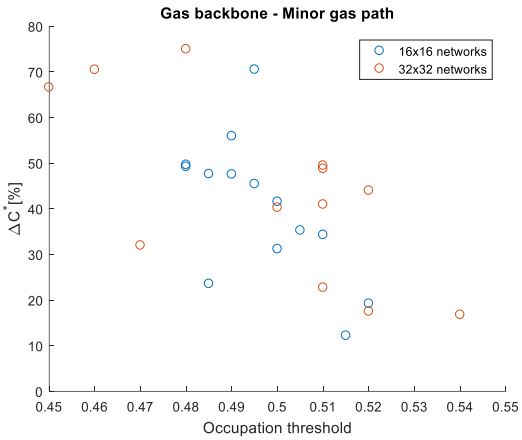

Figure 7.5(a): Difference between the gas backbone and minor gas path as a percentage; cases from appendix B1 and B2.

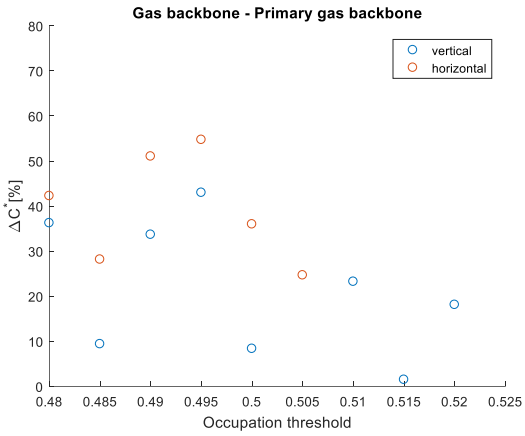

Figure 7.5(b): Difference between the gas backbone and primary gas backbone; cases from appendix B1. 16x16 Networks.

Comparing the difference in accuracy of the minor gas path and primary gas backbone is not necessarily apt since the primary gas backbone is defined arbitrarily. Determining the minor gas path is easy and most suited for networks with a high occupation threshold.

Tortuosity and parallel flow

The conductivity of the gas backbone is computed for twelve 32x32, networks with occupation thresholds ranging from 0,45 to 0,54. The results are plotted versus the pore specific bond resistances in figure 7.6(c) and particular attention is given to the network conductivity with pore aspect ratio of $\mathrm{b/a} = 2{,}2$ in figures 7.6(a) and (b).

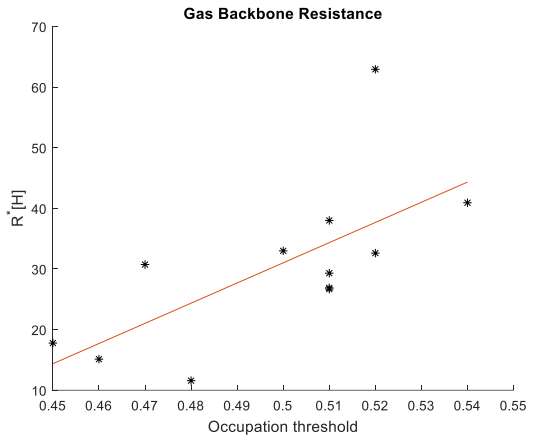

Figure 7.6(a): Network resistivity of twelve 32x32, networks with a pore aspect ratio of b/a=2,2 and bond resistance of 1H; cases from appendix B2

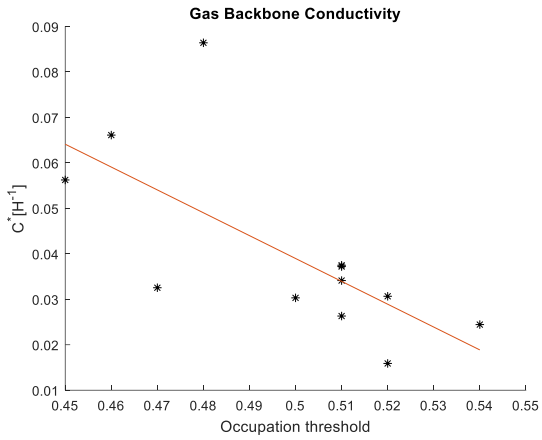

Figure 7.6(b): Network conductivity of twelve 32x32, networks with a pore aspect ratio of b/a=2,2 and bond conductivity of $1H^{-1}$; cases from appendix B2

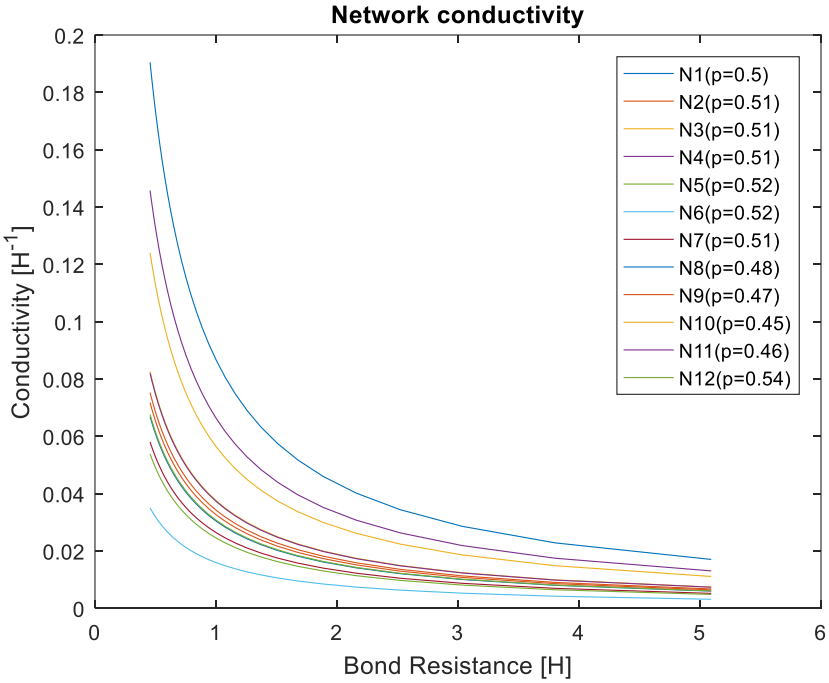

Figure 7.6(c): Network resistivity of twelve 32x32 networks for every given bond resistance; cases from appendix B2

Data from the 32x32 networks reaffirms the findings from the 16x16 networks that the network conductivity decreases with increased occupation threshold from a decrease in gas occupancy. Network conductivity is found to be a function of the amount of parallel flow and tortuosity.

As mentioned previously, parallel flow contributes positively to the conductivity of the network. As the occupation threshold increases fewer conducting bonds are activated and fewer parallel paths are established ensuing in a marked decrease in conductivity. The contribution of parallel paths is illustrated by the difference in conductivity of the minor gas path and gas backbone in figure 7.5(a). Additionally, figures 7.7(a) through (d) also illustrate how reducing the threshold for a given network increases the amount of connections and parallel paths and therefore also increases the conductivity of the lattice.

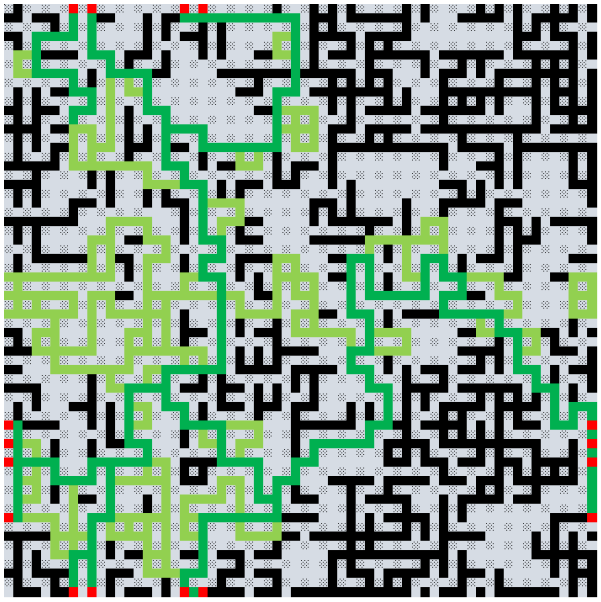

Figure 7.7(a): Network 6 (p=0,50; b/a=2), $\mathrm{C_{WE}} = 0.0186\mathcal{H}^{-1}$

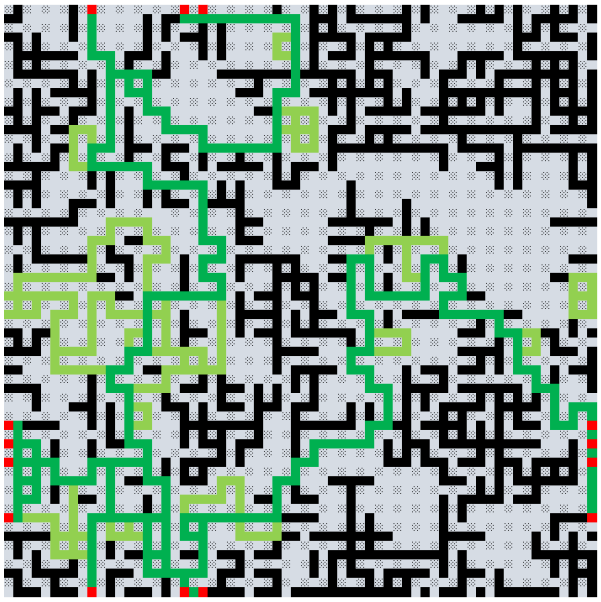

Figure 7.7(b): Network 6 (p=0,52; b/a=2), the amount of flow paths is reduced to three and three major connections in the middle, second- and third quadrant are eliminated. Conductivity decreases to $\mathrm{C_{WE}} = 0{,}0138\mathcal{H}^{-1}$

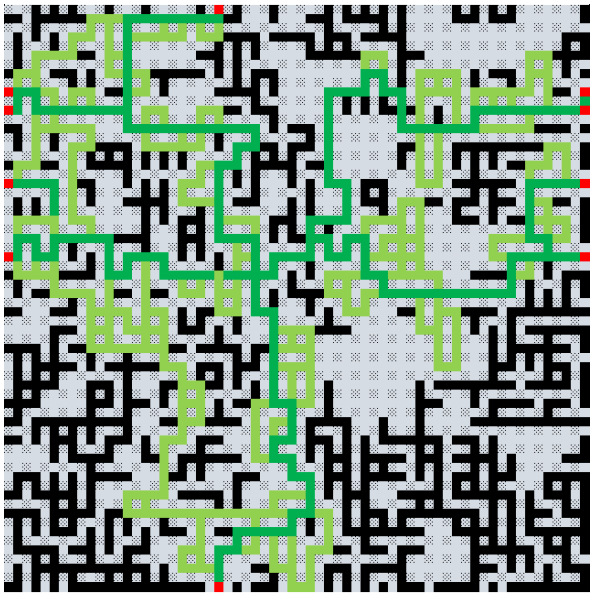

Figure 7.7(c): Network 2 (p=0,50; b/a=2)
$C_{NS} = 0{,}0414\mathcal{H}^{-1}$

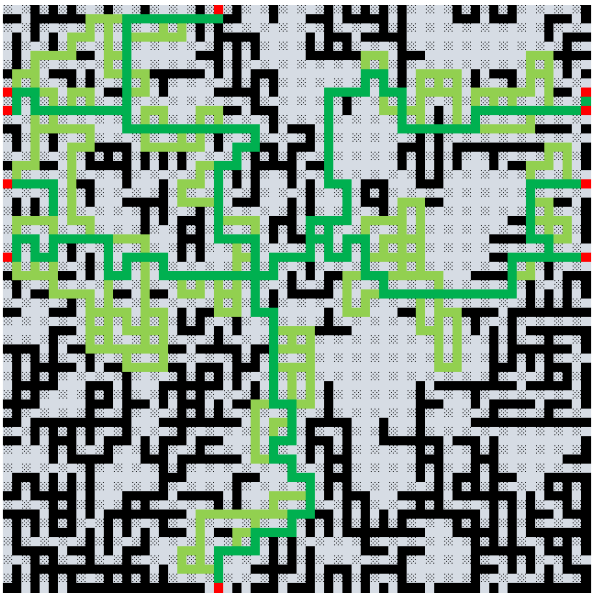

Figure 7.7(d): Network 2 (p=0.51; b/a=2), the amount of flow paths remains the same but a connecting path in the third quadrant is eliminated. Conductivity reduces to
$C_{NS} = 0{,}0296\mathcal{H}^{-1}$

Secondly, the tortuosity of the flow paths is proportional to the network resistivity. The longer the length of the flow path the more tortuous it is and the higher the resistance will be. The length between the terminal nodes is determined (i.e. the minor gas path) to calculate each path's tortuosity. From figure 7.8(a) below it can be seen that network resistivity is proportional to the tortuosity. Plotting the occupation threshold versus the tortuosity in figure 7.8(b) shows that the tortuosity of a network is random and independent of the occupation threshold of the networks.

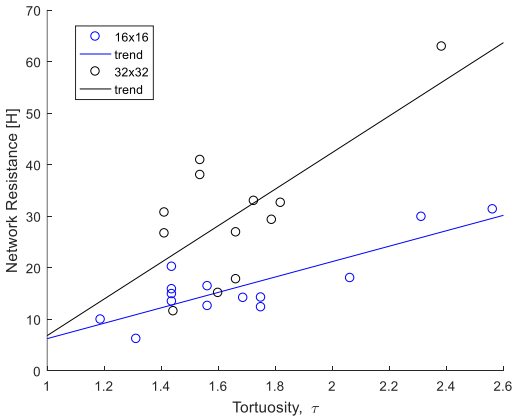

Figure 7.8(a): Network resistance is proportional to the tortuosity of the minor gas path; cases from appendix B1 and B2.

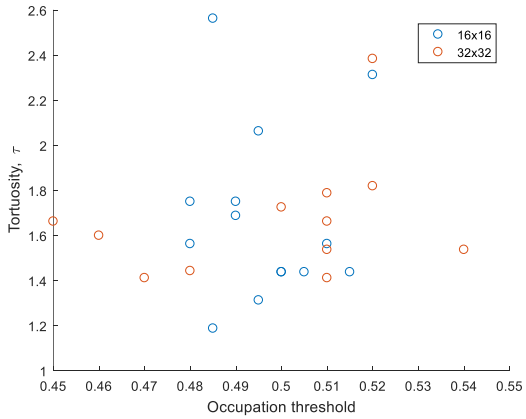

Figure 7.8(b): Tortuosity of the minor gas path is independent of the occupation threshold of the network; cases from appendix B1 and B2.

The exact extent to which tortuosity and parallel flow contribute to the total conductivity of the network is indeterminable due to the randomness of lattice percolation. For higher occupation thresholds the tortuosity has more influence and parallel flow has less.

7.2. Liquid network conductivity

The liquid conductivity is determined for each network in the same direction as the gas conductivity for the twelve 32x32, networks. Results in figure 7.9 indicate that the liquid conductivity is proportional to the occupation threshold.

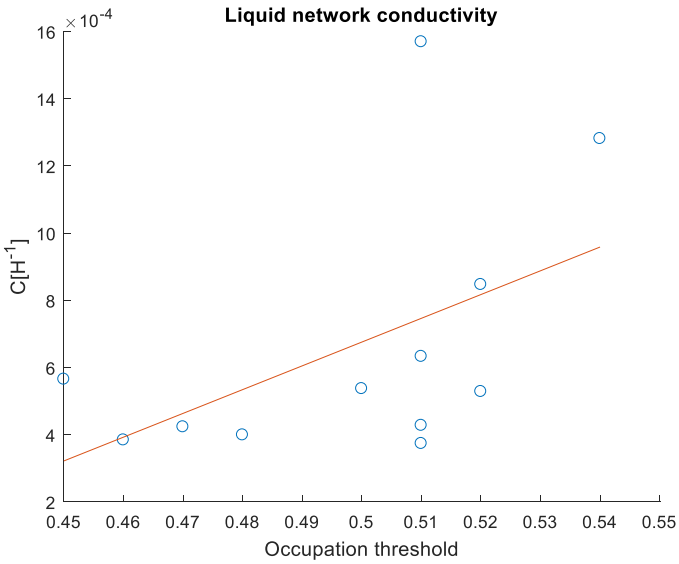

Figure 7.9: liquid conductivity of the 12 networks; cases from appendix B2.

As the occupation threshold increases so does the liquid conductivity because gas clusters are allowed to span less of the lattice and more space is inevitably created for liquid flow. This is similar to how the liquid saturation increases/decreases if the gas saturation decreases/increases. The conductivity of every path is calculated as the sum of the products of resistivities and their number of occurrences, n (see Eq. 7.1). Paths are defined so that number of liquid bridges is minimized.

$$\mathrm{R_{path}} = (\mathrm{n_1} \times 172\mathcal{H}) + (\mathrm{n_2} \times 229\mathcal{H}) + (\mathrm{n_b} \times 444\mathcal{H});\ (7.1)$$

Figure 7.10 breaks down the distribution of the number n's and their path conductivity. The most common element by far is the 90° turn $(\mathrm{R_1})$ so even though it has a low value it contributes the most to the resistance of liquid path.

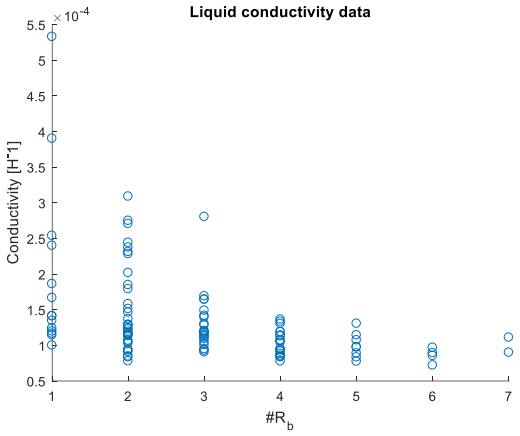

Figure 7.10(a): Conductivity of the liquid flow paths versus the number of liquid bridges, R_b, elements; cases from appendix B2.

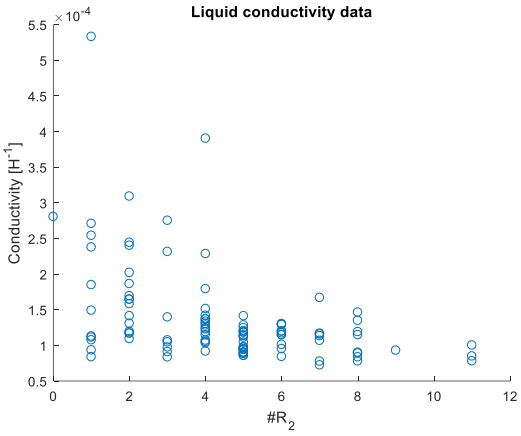

Figure 7.10(b): Conductivity of the liquid flow paths versus the number of straight-ahead, R_2, liquid movements; cases from appendix B2.

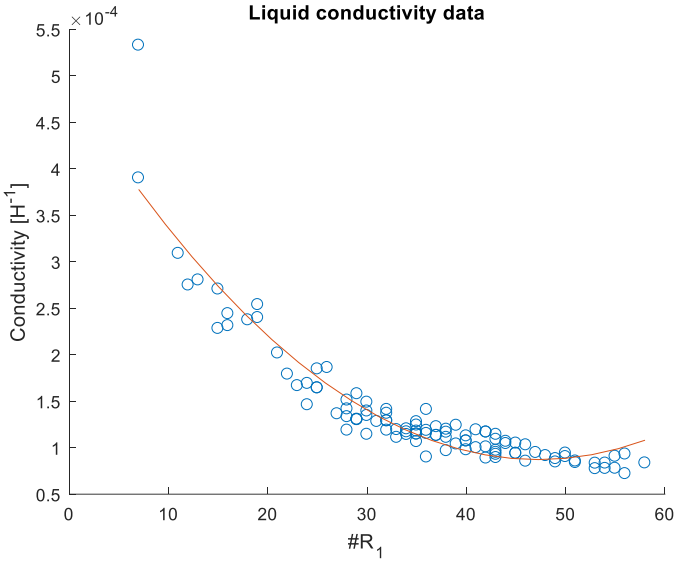

Figure 7.10(c): conductivity of the liquid flow paths versus the number of 90-degree turns, R_2, for liquid; cases from appendix B2.

7.3. Ratio of liquid and gas conductivity

The ratio of the liquid and gas conductivity for a pore throat of aspect ratio 2.2 is calculated for twelve 32x32 networks. The liquid conductivity is found to be about 1/100 that of the gas conductivity (see Fig. 7.11) and when adjusted for a viscosity difference between gas and water of about 10 times then the liquid conductivity is 1/1,000 to 1/10,000 that of the gas conductivity (see Fig. 7.12).

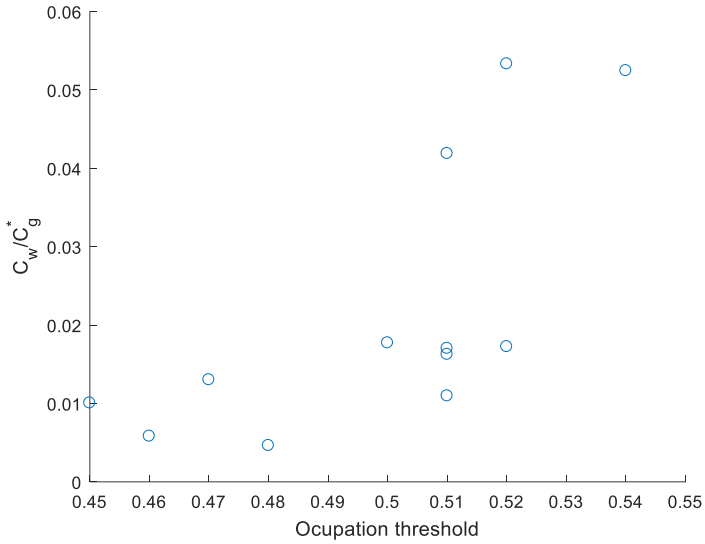

Figure 7.11: Ratio of the liquid and gas conductivity for twelve 32x32 networks; cases from appendix B2.

Two types of gasses are applied to the results in figure 7.11. The first is nitrogen at room temperature and atmospheric pressure $(\mu = 0.019\text{cp})$ and the second is supercritical CO_2 $(\mu = 0{,}068\text{cp})$. Nitrogen is commonly used in microfluidic experiments on foam generation and is also used in Kovscek et al.'s (2007) experiment. CO_2 at reservoir conditions is supercritical and occurs in enhanced oil recovery and CO_2 storage. Nitrogen's viscosity is about 1/55 that of water and the liquid conductivity for all but two values is 1/10,000 of the gas conductivity. The liquid conductivity for supercritical CO_2 is 1/1,000 that of the gas conductivity.

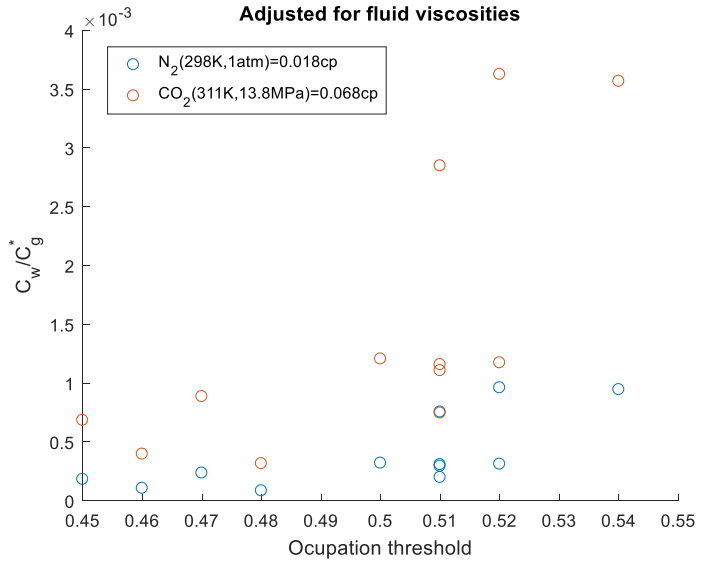

Figure 7.12: Ratio of the liquid and gas conductivity for 12, 32 by 32, networks adjusted for the viscosity of water and gas; cases from appendix B2.

8. Applications of foams in applied earth sciences

Foam generation mechanisms and foams are used in a number of ways in reservoir engineering. During enhanced oil recovery foams are utilized to improve the sweep of the reservoir. Other applications include CO_2 storage and environmental remediation where foams are utilized to increase capillary trapping and plug high-permeability zones to prevent the spread of contaminant.

8.1. Enhanced oil recovery (EOR)

In enhanced oil recovery (EOR) gasses such as steam or CO_2 are injected into the reservoir to increase recovery in mature reservoirs. A problem that can occur is poor sweep efficiency and high gas-oil ratios resulting from the formation of preferential flow paths to the production well. This is referred to as gas breakthrough and results in the gas only contacting a small portion of the reservoir (Rossen, 1996). Breakthrough occurs from viscous fingering, gravitational segregation and/or thief zones (high permeability zones) (Rognmo, 2018). Foams increase sweep efficiency in two ways. First, by reducing the gas mobility and second by plugging a portion of the reservoir so that fluids are diverted to another, unswept, part of the reservoir.

Liquid lamellae stabilize when surfactant is introduced into the reservoir, leading to greater foam generation and a reduction of gas mobility (Almajid & Kovscek, 2019; Rossen, 1996). Gas mobility, λ_i, is the product of permeability (k) and relative permeability (k_i) divided by fluid viscosity, μ_i (eq. 8.1). When gas mobility is reduced the gas flow rate, u_{gas} (eq. 8.2), is also reduced as well.

$$\lambda_i = \frac{k_i(S_i)k}{\mu_i}; \ (8.1)$$

$$u_i = -\lambda_i \nabla p; \ (8.2)$$

The effect of foam on the gas mobility is due to both an increase in the effective viscosity and a decrease in relative permeability which is a function of the fluid saturation, S_i (Almajid & Kovscek, 2019).

During plugging, foam is applied to unproductive reservoir layers at the injection or production well in order to redirect flow patterns within the reservoir. At the injection well liquid flow is diverted to target layers while at the production well unwanted reservoir fluids are prevented from entering the production stream (Rossen, 1996).

8.2. Subsurface CO_2 storage

Carbon capture and storage (CCS) is a promising method to reduce anthropogenic CO_2 emissions by capturing it and storing it safely and permanently in subsurface reservoirs. These reservoirs can be saline aquifers, mature- or depleted hydrocarbon reservoirs. The three main trapping mechanisms are structural trapping, dissolution trapping and capillary (aka residual) trapping.

Capillary trapping is significant in water saturated media and is similar to the flow problem studied here because gas penetrates the medium, establishes a network and experiences repeated snap-off. In a sense a discontinuous gas phase is generated like a foam. Therefore, attention is concentrated on the capillary trapping mechanism.

During CO_2 sequestration in strongly water wet reservoirs the gas is trapped within the pores of the network as bubbles (also known as ganglia) surrounded by liquid. This process of capillary trapping is considered as one of the most important trapping mechanisms for CO_2 trapping in water-saturated reservoirs (Krevor et al., 2015; Raza et al., 2018). Capillary trapping occurs when gas penetrates the pores and snap-off occurs at the rear pore throat thus rendering the gas immobile and ensuring safe and permanent storage of the CO_2. Direct pore-scale observations by Krevor et al. (2015) with 3D CT imaging found that trapped saturations of gas will be at least 10% in a water saturated medium or in other words, 30% of the pore volume. Furthermore, Iglauer et al. (2011) introduce an empirical relation to quantify the capillary trapping capacity. To calculate the capillary trapping capacity per unit of rock the product of porosity and residual gas saturation is taken. Their gathering of data suggests a maximum trapping capacity of 11% for a porosity of 0,22. After CO_2 injection, gas migrates through the reservoir as a mobilized foam where lamellae migrate through the pore space as a sort of a "bubble train". At the front of the plume piston-like advance invades water-saturated pores while at the trailing edge of the plume capillary pressure reduces and snap-off occurs thus trapping the gas as the water is imbibed back into the pore space (Krevor et al., 2015; Rossen, 1996).

8.3. Combining CCS and EOR with foams

Carbon capture and storage has the potential to help decarbonize carbon intensive processes such as steel, cement and energy production. However, the low price of CO_2 and the cost of capture and transport pose a significant financial barrier to CCS. One way to tackle this issue is to create a market price for CO_2 but it is also possible to lower the cost of CCS by combining it with enhanced oil recovery (Clark & Santiso, 2018; Føyen et al., 2020; Roefs et al., 2019). Roefs et al. (2019) determined with an environmental economic trade-off analysis that combining EOR with CO_2 storage followed by just storage would increase overall costs of a project but decrease global warming potential while still remaining profitable. An important consideration for an eventual project is how to approach co-optimization. Co-optimization in a project development context can have the goal of either optimizing the net present value, production, storage or both production and storage (Wang et al., 2018). Here, co-optimization is considered in the sense of production-storage optimization within the bounds of the economic reality of things.

Jessen et al. (2005) found that breakthrough time and cycling are both important design considerations for storage and production. Although CO_2 storage increases substantially after breakthrough, the costs associated with cycling the gas back into the reservoir make it an

economically unattractive solution for co-optimization (Jessen et al., 2005; Wang et al., 2018). A number of engineering decisions can be made that address CO_2 storage optimization and also delay breakthrough. These are: the implementation of partial completions of the wells and the use of water alternating gas (WAG) injection. Breakthrough typically occurs through high permeability thief zones that form preferential flow paths for fluids. With a partial completion of the injection well direct injection into these zones is avoided and with WAG injection water is meant to occupy their space instead of the gas. A lower completion of the injection well increases gas dispersion which in turn increases storage. Another advantage of a lower completion of the production well is that it increases the time before breakthrough. In addition to this the lower completion of the production well also reduces the gas-oil ratio and therefore reduces cycling costs (Jessen et al., 2005).

Rezk et al. (2019) found from sample flooding experiments of sandstone that high injection rates favor oil production but decrease storage efficiency. Conjointly, the experiments determined that storage efficiency and oil production are drastically aided by vertical flooding due to gravity-assisted gas drainage as opposed to horizontal flooding. These results are reflected in Ahmadi et al.'s (2016) reservoir simulation which also take gravitational segregation into account. They simulate three different CO_2 injection schemes where CO_2 is injected in the oil-column, in an underlying aquifer and in both together. All three scenarios are carried out with a fixed injection rate defined as the critical injection rate, which is the injection rate where the recovery factor of the reservoir no longer increases with an increase in injection. The results indicate that an equal combination of aquifer and oil-column injection has the best oil recovery factor, while aquifer injection has the best sequestration ratio. Theoretically, this increase in oil production is due to the sweeping of the capillary transition zone from gravitational segregation (Jessen et al., 2005) but the simulation does not take the economic drawback of gas breakthrough into account and thus the purported figures for sequestration ratios are a poor indicator for a real project.

Of specific interest is the applicability of foams to aid CO_2 storage in hydrocarbon reservoirs either as a tool to prevent breakthrough or by directly improving storage capacity of the reservoir.

Indeed, there exists potential for foams to aid CO_2 storage within the reservoir. The ability of foams to plug thief zones is known from EOR and the reduction of gas mobility aids gas dispersion within the reservoir volume. An added benefit of decreased mobility is that dispersion decreases the risk of damaging the reservoir seal from repressurization of depleted hydrocarbon reservoirs or saline aquifers.

The use of surfactant to generate stronger foams increases the capacity for capillary trapping within water wet reservoirs. Foyen et al. (2019) conducted CO_2 flooding experiments on sandstone cores with different surfactants and found that CO_2 capacity increased by 27% with the application of foam. The introduction of surfactant helps increase lamellae stability and enables

the gas to enter smaller pore throats. Then, upon arrival within the smaller pore space gas gets trapped from capillary trapping.

The economic reality of CO_2 injection in EOR is that increasing the injection rate of CO_2 indefinitely to maximize oil recovery and storage is not possible. The costs of supply, transport and cycling would simply decrease the profitability of the project. The ideal injection scheme for the project would therefore prioritize delaying breakthrough while still optimizing storage and production. To this extent a lower completion of the well within the oil-column or in an eventual aquifer would be beneficial for delaying breakthrough while also increasing storage.

8.4. Modeling of heterogeneous media

The process of capillary trapping and foam generation is considered on a microscopic, pore-scale level with a model tailored specifically to consider steady state flow in homogeneous media. This model is made from a periodic lattice (constant coordination number) and a uniform bond conductivity. However, porous media are inherently heterogenous so some adaptation of the model is required in order to take into account a heterogeneous three dimensional medium. Generally, to model flow in heterogenous media the distribution of pore-scale attributes needs to be observed for application to a network model.

To start, the lattice is extended to the third dimension by using a 3D cubic lattice with a coordination number of 6. This assumes that the coordination number is uniform so alternatively a statistical distribution of the pore coordination numbers can be applied. However, doing this leads to the problem that the percolation threshold for such an irregular network is unknown (Hunt & Sahimi, 2017).

The conductance values of each bond are proportional to their radius so by determining the size distribution of pore throats it is possible to determine the pore throat conductivities for each throat. To do this, first, the normalized pore size distribution is applied to the network as the probability (p) and thereafter the percolation threshold (p_c) is subtracted from it to find the bond probability of each throat (Selyakov & Kadet, 1997). Furthermore, the bond probability is then utilized as an edge attribute to calculate the equivalent conductivity of the network graph. The required statistical description of the medium can be determined in a number of ways. The simplest of which is conventional image analysis and the more advanced is micron scale CT imaging (Hunt et al., 2014).

Blunt (p. 32-56, 2017) and Hunt & Sahimi (2017) give an overview for the different techniques available for pore-scale representations of porous media as transport networks. In these techniques the pore network is constructed either from an underlying statistical description or directly from an image of the pore space. Methods that stand out are: Voronoi polygonization, medial axis skeletonization and voxelized approximation. Almajid et al. (2019) utilize a statistical pore network and the invasion percolation algorithm with memory to model the dependence of

the flowing foam fraction on the pressure gradient. In their model pore throat radii are assigned according to a Rayleigh distribution.

To model foam generation with Roof snap-off it is worth considering the ratio of the pore throat size and pore size. The ratio directly influences the likelihood of Roof snap-off where a high ratio makes snap-off more likely. Commonly, the size of the pores in a network are scaled from the size of the pore throats (Hunt, 2014) but doing this would not allow determination of snap-off sites. Almajid et al. (2019) model snap-off randomly but if pore size data is available it may be used to determine where snap-off is likely to occur.

8.5. Environmental remediation

Foam technology is known within the oil and gas industry but can also be used for aquifer (Hirasaki et al., 1997) and soil remediation (Atteia et al., 2013; Portois et al., 2018; Wang & Mulligan, 2004). Contaminants such as dense non-aqueous phase liquids (DNAPL) are difficult to remove with traditional techniques because of the inherent chemical properties of DNAPL's and poor sweep efficiency of traditional techniques. DNAPL's have a low solubility, high density, high interfacial tension and adsorption to soil matrix (Atteia et al., 2013; Hirasaki et al., 1997; Mamun et al., 2002a; Portois et al., 2018; Wang & Mulligan, 2004). Heterogeneous permeability distribution of the reservoir and gravity segregation of injected fluids lead to poor sweep efficiency of the reservoir (Marmun et al., 2002a). These problems are known in EOR and foams are used in essentially the same way for aquifer and soil remediation purposes. Foam in environmental remediation is used as a blocking agent and as a tool for flushing.

Foam is used as a blocking agent to confine a source zone of contaminant by drastically reducing the permeability of the surrounding area. In EOR-jargon this is called plugging of the thief zone. Laboratory and field experiments by Portois et al. (2018) found that foam reduces the relative water permeability k_{rw} by a factor of 100-1000. The determining factor for k_{rw} is the quality of the foam, high quality foams reduce the water saturation by the most and consequently the relative permeability of water is reduced accordingly (Portois,2018).

During flushing, foam is selectively applied to high permeability layers to direct flow of surfactant to the higher permeability layers for flushing. In situ generation of foam within these regions improves the displacement process of DNAPL contaminant by reducing the gas mobility (Hirasaki et al., 1997; Mamun et al., 2002a). Hirasaki et al. (1997) have successfully used mobility control for aquifer remediation in the USA. In the field, foam was used to plug an overlying sand layer (thief zone) to divert surfactant solution to the contaminated zone.

Another benefit of foams is that It can reduce the costs of pump-and-treat methods because less surfactant will be needed. Surfactants are also used in pump-and-treat operations to decrease interfacial tension and increase the solubility of NAPL's (Atteia et al., 2013; Wang & Mulligan, 2004). Additional considerations for design planning are what the foam quality, stability and injection pressure will be.

Foam quality, can be measured as the ratio of gas volume and foam volume. The greater the ratio the better the quality of the foam. Foams of greater quality reduce the relative permeability of water by the most.

Although foams are thermodynamically unstable, they can be made to last a long time, in the order of months. However eventually foams will degrade due to coalescence so at this point they either need to be maintained or replaced (Portois et al., 2018; Wang & Mulligan, 2004).

Soil remediation occurs at a shallow depth. Therefore, the allowed amount of injection pressure is limited relative to gas and oil operations. CO_2 is more suitable than nitrogen gas as it allows lower injection pressures (Portois et al., 2018).

9. Conclusion and recommendations

9.1. Conclusion

Foams are an important tool for reservoir applications which can help oil recovery, improve carbon storage and expediate aquifer/soil remediation. However, observations from 2D experiments are used in mechanistic modeling of steady foam generation in 3D media. In this report the conductivity of gas and liquid in a 2D micromodel is estimated from a representative homogenous 2D percolation model. This is done in order to determine the viability of steady state two-phase flow within a micromodel. Conductivity was estimated for a pore network with a rectangular geometry where liquid flows in the pore throat's corners while gas occupies the center. A new unit for resistivity $\Delta P/Q$ is defined as $\mathcal{H}[\mu/R^3]$ and conductivity is its inverse. To enable two-phase flow within the 2D model liquid is allowed to cross gas-occupied pore throats as liquid bridges.

The behavior of the model is analyzed. The conductivity of the gas backbone decreases with increased occupation threshold. The occupation thresholds of the models are random and considered at the point where gas flows in the vertical and horizontal directions. The gas conductivity decreases while the liquid conductivity increases with an increase in occupation threshold. Conductivity of the gas backbone is a function of the amount of parallel flow paths and path tortuosity.

From observations of the networks and by comparison of the network conductivity to the conductivity of the minor gas path it is determined that networks with low occupation thresholds have a higher gas conductivity due to an increased number of parallel flow loops. To the contrary, networks with high occupation threshold have fewer parallel flow paths so the liquid flow is facilitated better and the liquid conductivity is higher.

The tortuosity for a given network at the occupation threshold is measured from the length of the minor gas path and it is found that the tortuosity of the models is independent of the occupation threshold. The influence that the tortuosity has on the gas conductivity increases with greater occupation threshold because there is less parallel flow. As a result, the estimation of gas conductivity with the minor gas path is better for networks with high occupation thresholds.

The magnitude of the gas conductivity and liquid conductivity are reported and compared as a ratio. The values reported are for pore geometry of aspect ratio 2,2 and a fixed width of twice the pillar radius. For this pore geometry the resistivity for gas in a throat is equal to $1\mathcal{H}$. The liquid resistivities on the pore-scale are defined generously (maximum allowed amount of liquid flow) for three characteristic movements: the 90-degree turn R_1, straight-ahead R_2 and the liquid bridge R_b. The resistivities for these movements are independent of the pore geometry and are equal to $172\mathcal{H}$, $229\mathcal{H}$ and $444\mathcal{H}$ respectively.

The results are first presented for a system where the fluid properties are undefined. The magnitude of the gas conductivity for both the 32x32 networks (appendix B2) and the 16x16 networks (appendix B1) is in of the order 10^{-2}. The liquid conductivity is only determined for the 32x32 networks and is considerably smaller with an order of magnitude between 10^{-3} and 10^{-4}.

Following from these results the ratio of the liquid and gas conductivity is of the order 10^{-2} but when adjusting for gas viscosity of nitrogen $(\mu = 0.019\text{cp})$ and supercritical CO_2 $(\mu = 0{,}068\text{cp})$ the ratio for liquid and gas conductivity is of the order 10^{-4} and 10^{-3}.

The results indicate that the liquid flow rate needed to achieve steady state (no fluctuation in pore occupancy) two-phase flow within a 2D micromodel is infinitesimal when compared to the gas flow rate. The allowed volume of liquid is so small that it is practically impossible to achieve steady two-phase flow without snap-off. Kovscek et al. (2008) conduct their experiment at steady state with a fractional gas flow (gas rate / total injection rate) above 0,9. This implies that the liquid flow rate for their results is about 1/10 the gas flow rate. However, results from this model indicate that such flow rates ensure snap-off.

9.1. Recommendations

The estimation of the resistances for both gas and liquid on the pore-scale assume that axial changes in pressure are negligible by taking $\mathrm{dP/dz}$ as a constant and dz equal to two times the radius of the pillar. Doing this, results in an estimation for flow resistivity in a throat shaped as a rectangular box. However, the surface geometry of the pore throat is not rectangular since the pillars are cylindrical.

An alternative to the proposed pore-scale estimations is to use flow simulation software that estimates the shape of fluid surfaces at different capillary pressure conditions. Work like this is currently being carried out by S.J. Cox of Aberystwyth University with the simulation software, surface evolver. Besides this the next bachelor thesis, by Ewald Obens, concerning this topic will also estimate the pore-scale fluid rates by using the program Comsol. His estimations of fluid rate and pressure difference can be used to define new pore-scale resistivities, $\Delta\mathrm{P/Q}$, for gas and liquid.

The new gas resistivity value can be multiplied times the equivalent resistivity of a network with bond resistivity 1H to estimate the new equivalent resistivity of the network. Similarly, the new liquid resistivities can be used in the same way as R_1, R_2 and R_b to calculate the new liquid network resistivity with relative ease.

Concerning the way that gas conductivity was calculated, two things could have been done differently.

First, in this paper the equivalent conductivity of the sample is calculated across the model by adding terminal nodes to the boundaries. However, the written scripts can calculate the equivalent conductivity between any two nodes and as long as the wrap-around boundaries are satisfied the equivalent network will be representative of the sample.

Second, the process of network generation and gas conductivity calculation could have been unified within MATLAB. Algorithms exist that can identify the gas backbone and separate it from the rest of the network (Hunt & Sahimi, 2017). Although, separating the gas backbone is not strictly necessary it is recommended since otherwise the node elimination script will be exceedingly slow and inefficient.

A. Bibliography

Ahmadi, M. A., Pouladi, B., & Barghi, T. (2016). Numerical modeling of CO2 injection scenarios in petroleum reservoirs: Application to CO2 sequestration and EOR. *Journal of Natural Gas Science and Engineering*, *30*, 38–49. https://doi.org/10.1016/j.jngse.2016.01.038

Almajid, M. M., & Kovscek, A. R. (2019). Pore Network Investigation of Trapped Gas and Foam Generation Mechanisms. *Transport in Porous Media*, *131*(1), 289–313. https://doi.org/10.1007/s11242-018-01224-4

Atteia, O., Del Campo Estrada, E., & Bertin, H. (2013). Soil flushing: a review of the origin of efficiency variability. *Reviews in Environmental Science and Bio/Technology*, *12*(4), 379–389. https://doi.org/10.1007/s11157-013-9316-0

Blunt, M. J. (2017). *Multiphase Flow in Permeable Media: A Pore-Scale Perspective*. Cambridge, United Kingdom: Cambridge University Press. https://doi.org/10.1017/9781316145098

Clark, J. A., & Santiso, E. E. (2018). Carbon Sequestration through CO2 Foam-Enhanced Oil Recovery: A Green Chemistry Perspective. *Engineering*, *4*(3), 336–342. https://doi.org/10.1016/j.eng.2018.05.006

Cox, S. (July, 2020). Email communication.

Derrida, B., Zabolitzky, J. G., Vannimenus, J., & Stauffer, D. (1984). A transfer matrix program to calculate the conductivity of random resistor networks. *Journal of Statistical Physics*, *36*(1–2), 31–42. https://doi.org/10.1007/bf01015724

Fogelholm, R. (1980). The conductivity of large percolation network samples. *Journal of Physics C: Solid State Physics*, *13*(23), L571–L574. https://doi.org/10.1088/0022-3719/13/23/001

Føyen, T., Brattekås, B., Fernø, M. A., Barrabino, A., & Holt, T. (2020). Increased CO2 storage capacity using CO2-foam. *International Journal of Greenhouse Gas Control*, *96*, 103016. https://doi.org/10.1016/j.ijggc.2020.103016

Frank, D. J., & Lobb, C. J. (1988). Highly efficient algorithm for percolative transport studies in two dimensions. *Physical Review B*, *37*(1), 302–307. https://doi.org/10.1103/physrevb.37.302

Hirasaki, G. J., Miller, C. A., Szafranski, R., Lawson, J. B., & Akiya, N. (1997). Surfactant/Foam Process for Aquifer Remediation. *International Symposium on Oilfield Chemistry*, 471–480. https://doi.org/10.2118/37257-ms

Hirasaki, G. J., Miller, C. A., Szafranski, R., Tanzil, D., Lawson, J. B., Meinardus, H., … Wade, W. H. (1997). Field Demonstration of the Surfactant/Foam Process for Aquifer Remediation. *SPE Annual Technical Conference and Exhibition*, 1. https://doi.org/10.2118/39292-ms

Holstvoogd, J. (2020). *Analysis of Steady Multiphase Flow in Porous Media: Across a Hypothetical 2D Percolating Network (Bachelor End Project)*. Delft, Netherlands: TU Delft.

Hunt, A., Ewing, R., & Ghanbarian, B. (2014). *Percolation Theory for Flow in Porous Media* (3rd ed.). New York, United States: Springer Publishing.

Hunt, A. G., & Sahimi, M. (2017). Flow, Transport, and Reaction in Porous Media: Percolation Scaling, Critical-Path Analysis, and Effective Medium Approximation. *Reviews of Geophysics*, *55*(4), 993–1078. https://doi.org/10.1002/2017rg000558

Iglauer, S., Wülling, W., Pentland, C. H., Al-Mansoori, S. K., & Blunt, M. J. (2011). Capillary-Trapping Capacity of Sandstones and Sandpacks. *SPE Journal*, *16*(04), 778–783. https://doi.org/10.2118/120960-pa

Jessen, K., Kovscek, A. R., & Orr, F. M. (2005). Increasing CO2 storage in oil recovery. *Energy Conversion and Management*, *46*(2), 293–311. https://doi.org/10.1016/j.enconman.2004.02.019

Kirkpatrick, S. (1973). Percolation and Conduction. *Reviews of Modern Physics*, *45*(4), 574–588. https://doi.org/10.1103/revmodphys.45.574

Knudsen, H. A., & Fazekas, S. (2006). Robust algorithm for random resistor networks using hierarchical domain structure. *Journal of Computational Physics*, *211*(2), 700–718. https://doi.org/10.1016/j.jcp.2005.06.007

Kovscek, A. R., Tang, G.-Q., & Radke, C. J. (2007). Verification of Roof snap off as a foam-generation mechanism in porous media at steady state. *Colloids and Surfaces A: Physicochemical and Engineering Aspects*, *302*(1–3), 251–260. https://doi.org/10.1016/j.colsurfa.2007.02.035

Krevor, S., Blunt, M. J., Benson, S. M., Pentland, C. H., Reynolds, C., Al-Menhali, A., & Niu, B. (2015). Capillary trapping for geologic carbon dioxide storage – From pore scale physics to field scale implications. *International Journal of Greenhouse Gas Control*, *40*, 221–237. https://doi.org/10.1016/j.ijggc.2015.04.006

Mamun, C. K., Rong, J. G., Kam, S. I., Liljestrand, H. M., & Rossen, W. R. (2002a). Extending Foam Technology from Improved Oil Recovery to Environmental Remediation. *SPE Annual Technical Conference and Exhibition*, 1. https://doi.org/10.2118/77557-ms

Mamun, C. K., Rong, J. G., Kam, S. I., Liljestrand, H. M., & Rossen, W. R. (2002b). Simulating use of foam in aquifer remediation. *Computational Methods in Water Resources, Proceedings of the XIVth International Conference on Computational Methods in Water Resources (CMWR XIV)*, 867–874. https://doi.org/10.1016/s0167-5648(02)80152-6

Portois, C., Boeije, C. S., Bertin, H. J., & Atteia, O. (2018). Foam for Environmental Remediation: Generation and Blocking Effect. *Transport in Porous Media*, *124*(3), 787–801. https://doi.org/10.1007/s11242-018-1097-z

Ransohoff, T. C., & Radke, C. J. (1988). Laminar flow of a wetting liquid along the corners of a predominantly gas-occupied noncircular pore. *Journal of Colloid and Interface Science*, *121*(2), 392–401. https://doi.org/10.1016/0021-9797(88)90442-0

Raza, A., Gholami, R., Rezaee, R., Bing, C. H., Nagarajan, R., & Hamid, M. (2018). CO2 storage in depleted gas reservoirs: A study on the effect of residual gas saturation. *Petroleum*, *4*(1), 95–107. https://doi.org/10.1016/j.petlm.2017.05.005

Redner, S. (2012). Fractal and Multifractal Scaling of Electrical Conduction in Random Resistor Networks. *Mathematics of Complexity and Dynamical Systems*, 446–462. https://doi.org/10.1007/978-1-4614-1806-1_29

Rezk, M. G., Foroozesh, J., Zivar, D., & Mumtaz, M. (2019). CO2 storage potential during CO2 enhanced oil recovery in sandstone reservoirs. *Journal of Natural Gas Science and Engineering*, *66*, 233–243. https://doi.org/10.1016/j.jngse.2019.04.002

Roefs, P., Moretti, M., Welkenhuysen, K., Piessens, K., & Compernolle, T. (2019). CO2-enhanced oil recovery and CO2 capture and storage: An environmental economic trade-off analysis. *Journal of Environmental Management*, *239*, 167–177. https://doi.org/10.1016/j.jenvman.2019.03.007

Rognmo, A. U. (2018). CO2-Foams for Enhanced Oil Recovery and CO2 Storage. Retrieved from https://www.researchgate.net/publication/332158061_CO2-Foams_for_Enhanced_Oil_Recovery_and_CO2_Storage

Rommes, J., & Schilders, W. H. A. (2010). Efficient Methods for Large Resistor Networks. *IEEE Transactions on Computer-Aided Design of Integrated Circuits and Systems*, *29*(1), 28–39. https://doi.org/10.1109/tcad.2009.2034402

Rossen, W.R. (1996). Foams in enhanced oil recovery. In R. K. Prud'homme & S. A. Khan (Eds.), *Foams theory, measurements, and applications* (pp. 413–445). New York, USA: Marcel Decker, inc. .

Rossen, William R. (2008). Comment on "Verification of Roof snap-off as a foam-generation mechanism in porous media at steady state." *Colloids and Surfaces A: Physicochemical and Engineering Aspects*, *322*(1–3), 261–269. https://doi.org/10.1016/j.colsurfa.2008.02.034

Rossen, W.R. (2003). A critical review of Roof snap-off as a mechanism of steady-state foam generation in homogeneous porous media. *Colloids and Surfaces A: Physicochemical and Engineering Aspects*, *225*(1–3), 1–24. https://doi.org/10.1016/s0927-7757(03)00309-1

Selyakov, V. I., & Kadet, V. (1997). *Percolation Models for Transport in Porous Media: With Applications to Reservoir Engineering (Theory and Applications of Transport in Porous Media (9))* (1997th ed.). Dordrecht, NL: Springer.

Serra, O. (2005). An isoperimetric method for the small sumset problem. *Surveys in Combinatorics 2005*, 119–152. https://doi.org/10.1017/cbo9780511734885.007

Wang, S., & Mulligan, C. N. (2004). An evaluation of surfactant foam technology in remediation of contaminated soil. *Chemosphere*, *57*(9), 1079–1089. https://doi.org/10.1016/j.chemosphere.2004.08.019

Wang, X., van 't Veld, K., Marcy, P., Huzurbazar, S., & Alvarado, V. (2018). Economic co-optimization of oil recovery and CO2 sequestration. *Applied Energy*, *222*, 132–147. https://doi.org/10.1016/j.apenergy.2018.03.166

Wu, F. Y. (1982). The Potts model. *Reviews of Modern Physics*, *54*(1), 235–268. https://doi.org/10.1103/revmodphys.54.235

Wu, F. Y. (2004). Theory of resistor networks: the two-point resistance. *Journal of Physics A: Mathematical and General*, *37*(26), 6653–6673. https://doi.org/10.1088/0305-4470/37/26/004

B. Appendix

B1. 16x16 Networks

In the left column are the networks created by Holstvoogd (2020) and in the right column is the network graph of their gas backbone. The gas backbone is highlighted in dark green in the left and in green on the right is the minor gas path of the network.

Network 1 (p=0,48)	
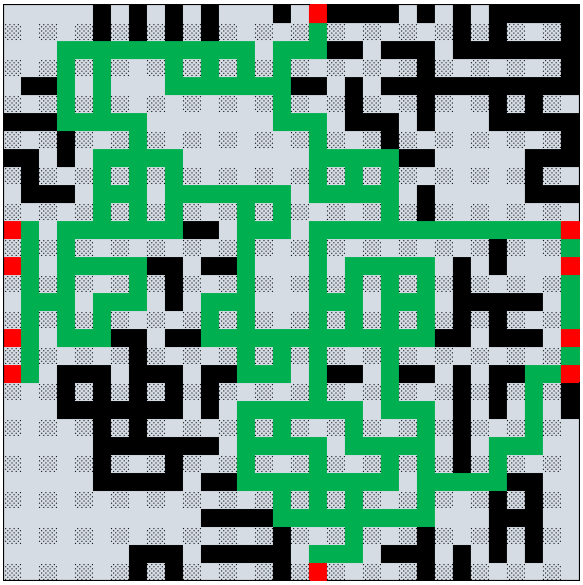	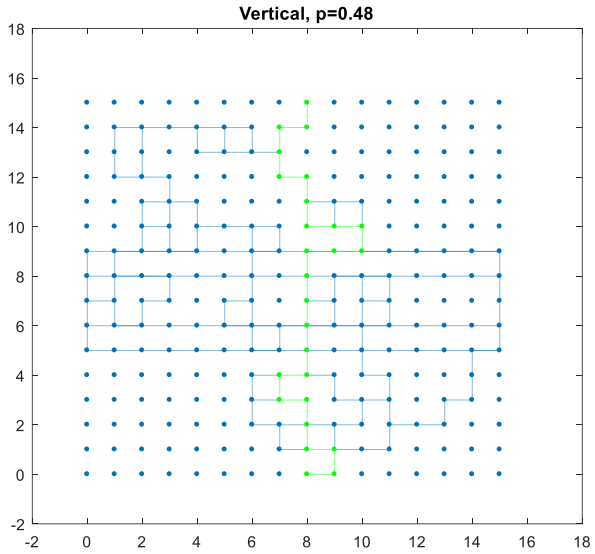 $C_v = 0{,}0794\mathcal{H}^{-1}$ $C_h = 0{,}0703\mathcal{H}^{-1}$
Network 2 (p=0,485)	
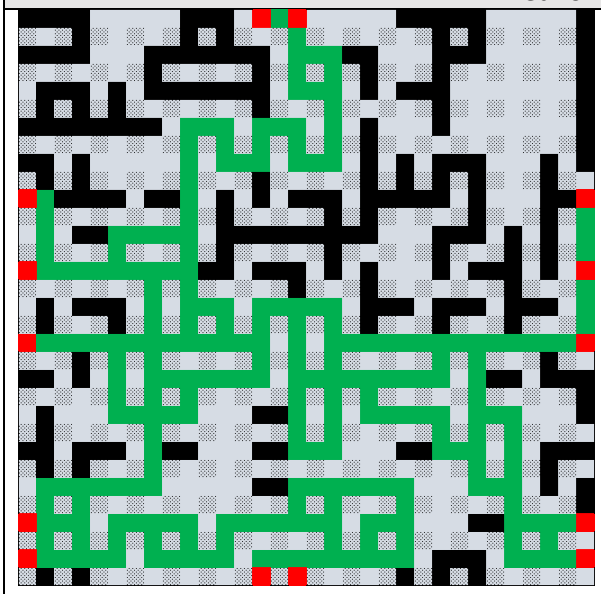	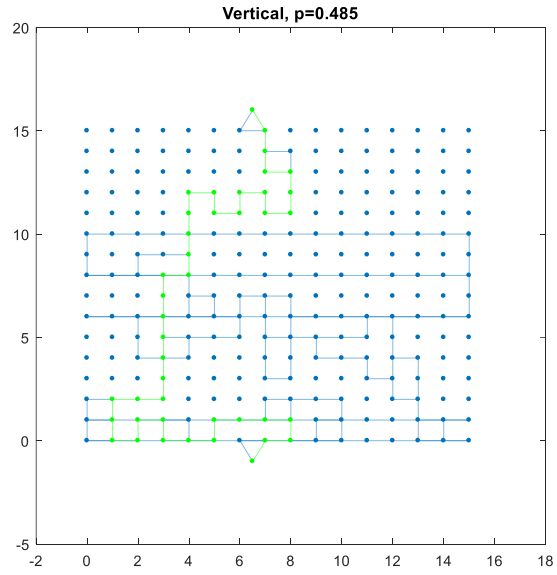 $C_v = 0{,}0319\mathcal{H}^{-1}$ $C_h = 0{,}1004\mathcal{H}^{-1}$

Network 3 (p=0,49)	
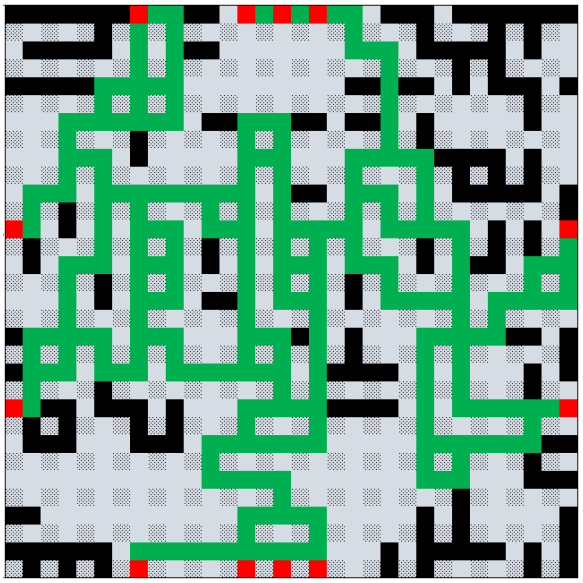	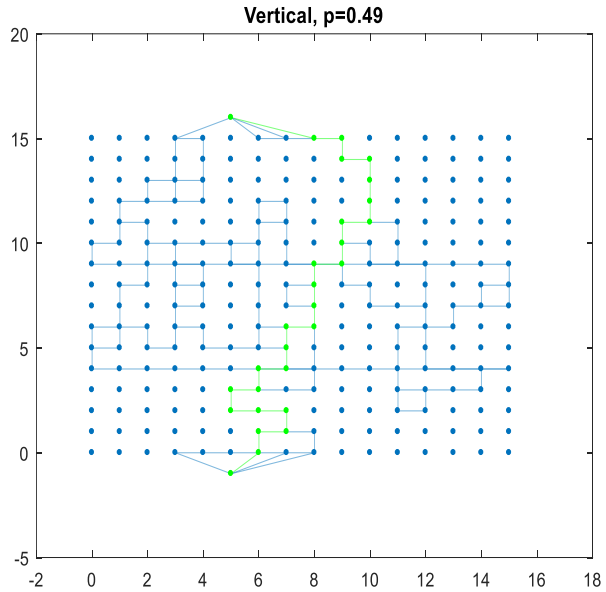 $C_v = 0{,}0706 H^{-1}$ $C_h = 0{,}0810 H^{-1}$
Network 4 (p=0,495)	
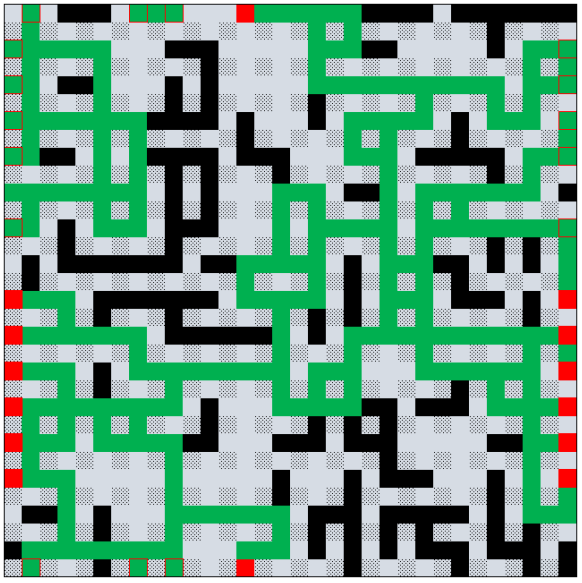	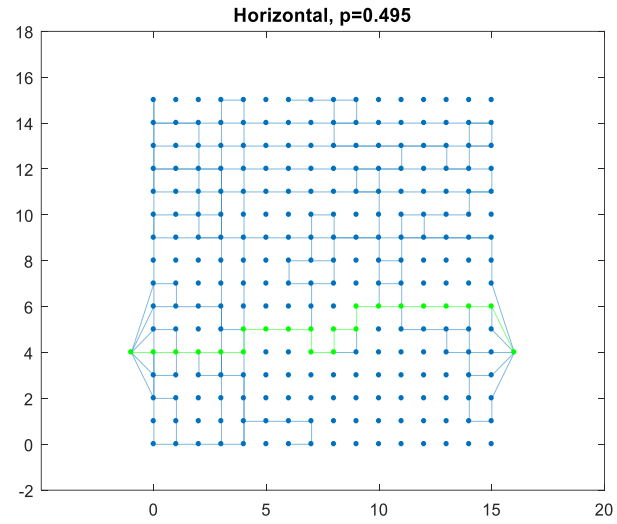 $C_v = 0{,}0555 \mathcal{H}^{-1}$ $C_h = 0{,}1633 \mathcal{H}^{-1}$

Network 5 (p=0,50)

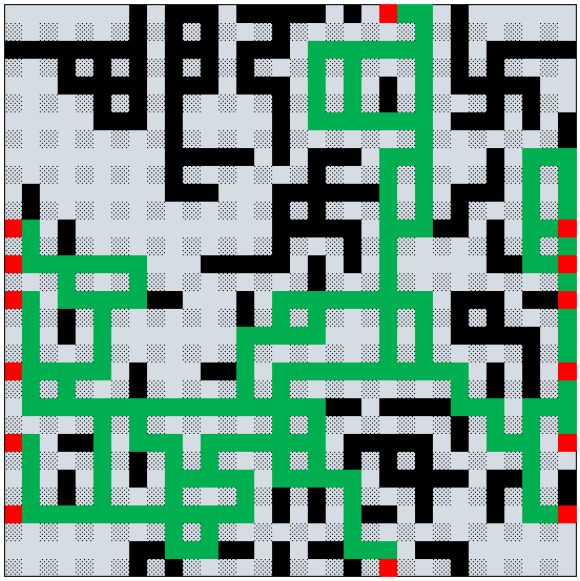

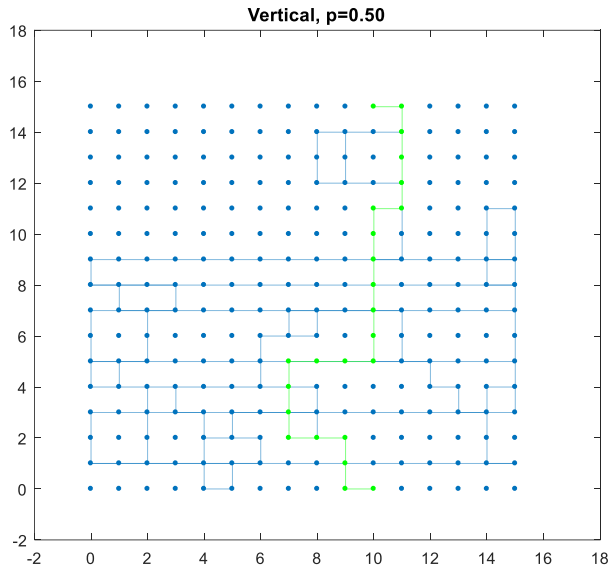

$C_v = 0{,}0632\mathcal{H}^{-1}$
$C_h = 0{,}0744\mathcal{H}^{-1}$

Network 6 (p=0,505)

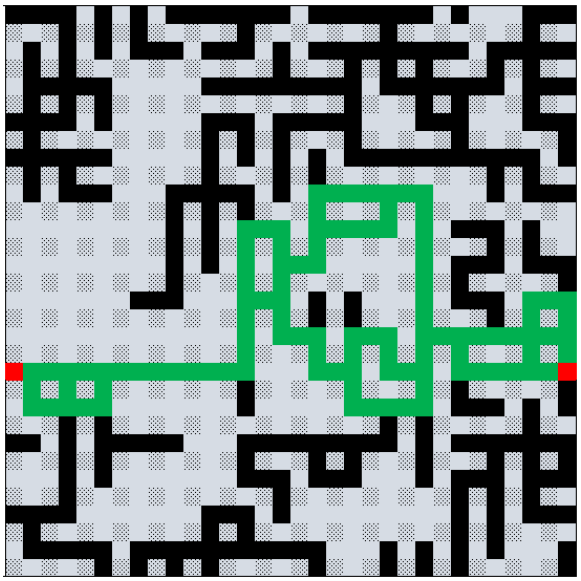

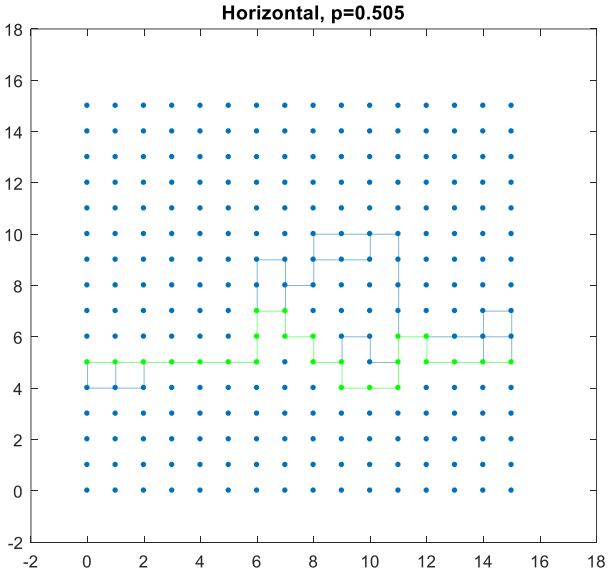

$C = 0{,}0671\mathcal{H}^{-1}$

Network 7 (p=0,51)

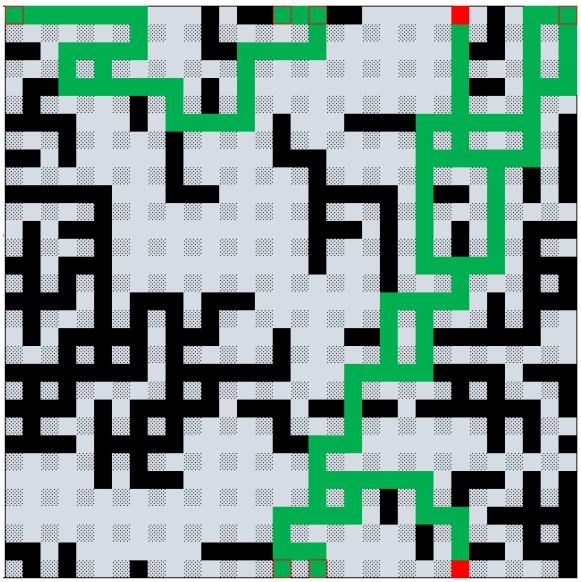

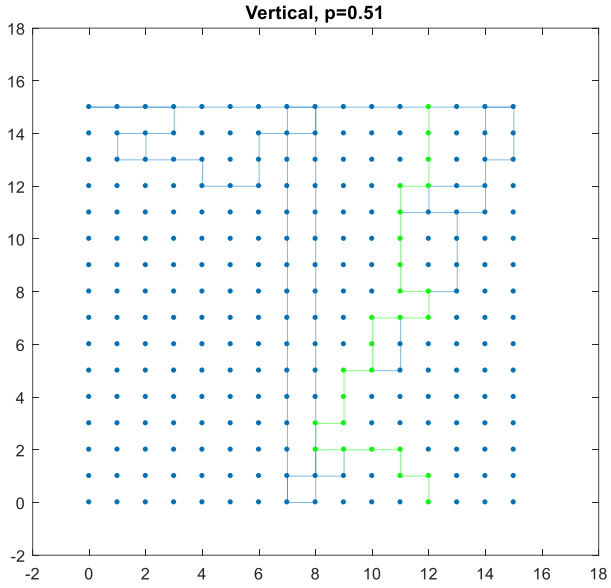

$C = 0{,}0609\mathcal{H}^{-1}$

Network 8 (p=0,515)

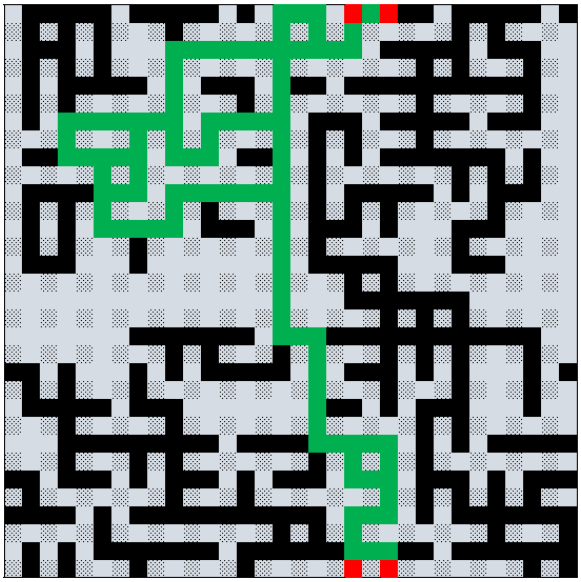

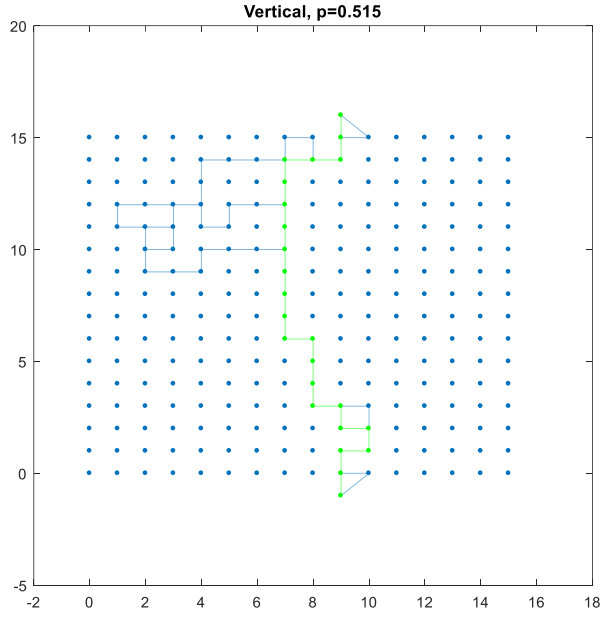

$C = 0{,}0495\mathcal{H}^{-1}$

Network 9 (p=0,52)

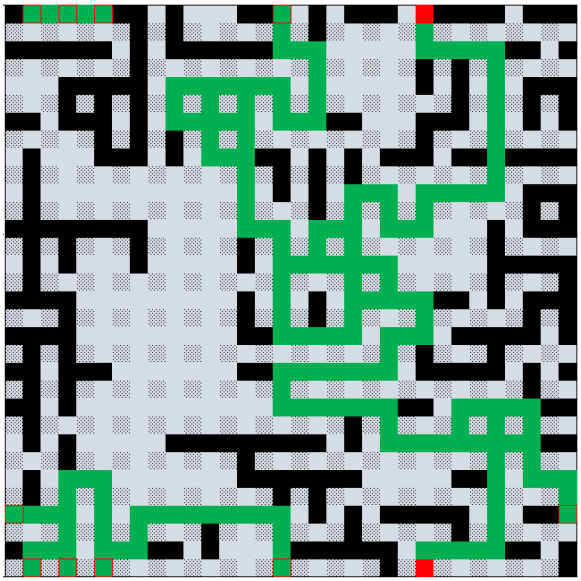

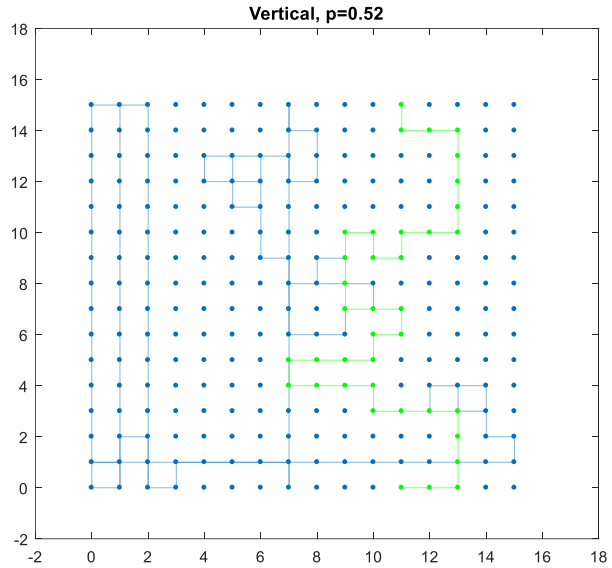

$C = 0{,}0335\mathcal{H}^{-1}$

B2. 32x32 Networks

The liquid paths and their corresponding conductivity data are presented per network in the right column. The gas conductivity graphs are given in the left column and their minor gas paths are highlighted in neon green.

Network 1(p=0,50)

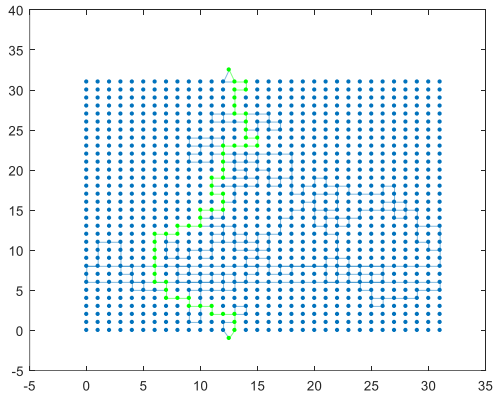

$C = 0.0303\mathcal{H}^{-1}$

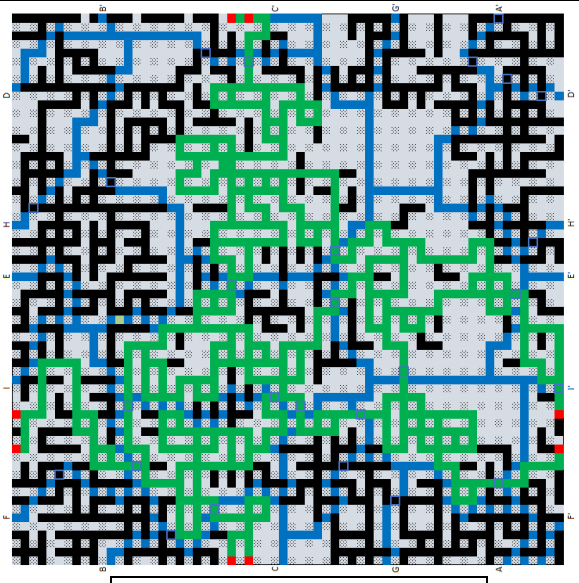

	R1	R2	Rb	C
Res	172	229	444	
DD'	26	2	1	0,00018608
II'	25	2	3	0,00016420
FF'	32	4	2	0,00013684
EE'	43	4	1	0,00011421
CC'	38	6	1	0,00011970

GG'	37	5	3	0,00011311
BB'	45	4	2	0,00010478
AA'	46	4	2	0,00010292
HH'	43	5	6	0,00008925

Network 2 (p=0,51)

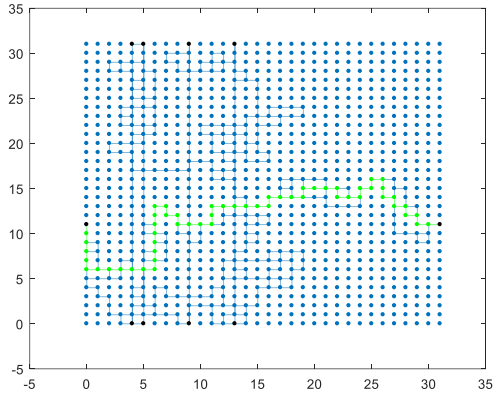

$$C = 0.0341 script H^{-1}$$

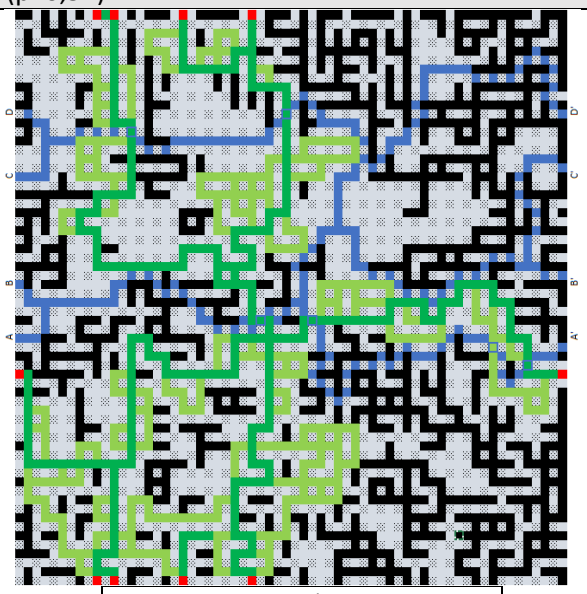

	R1	R2	Rb	C
Res	172	229	444	
AA'	42	5	2	0,00000358
BB'	33	5	1	0,00010803
CC'	27	9	3	0,00013765
DD'	30	8	2	0,00012442

Network 3 (p=0,51)

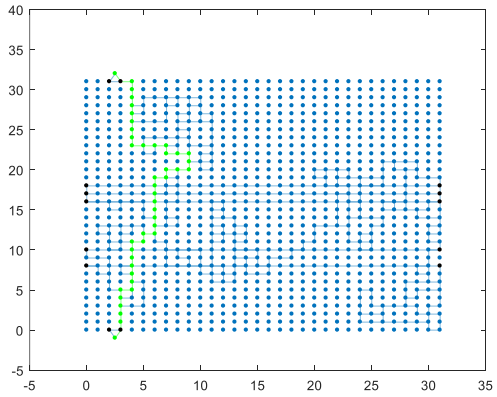

$$C = 0.0375 \mathcal{H}^{-1}$$

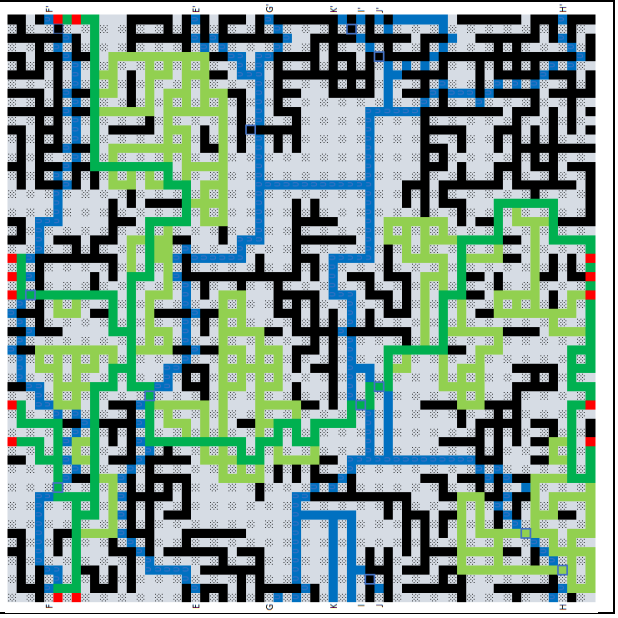

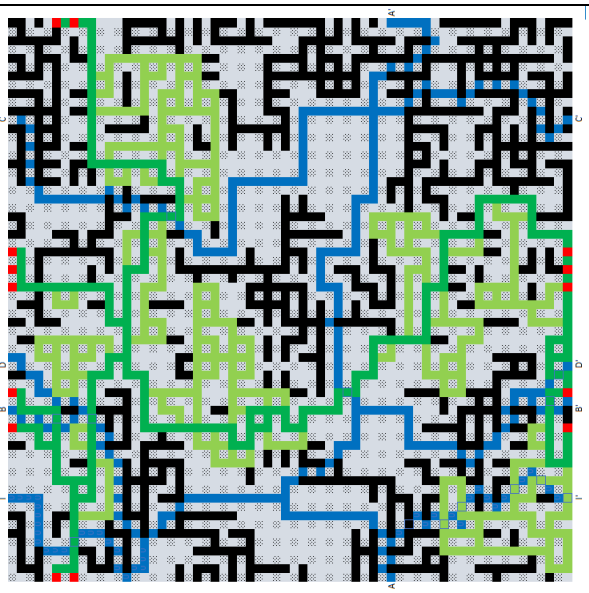

	R1	R2	Rb	C
Res	172	229	444	
KK'	13	0	3	0,000280269
II'	11	2	2	0,000308833
GG'	16	2	2	0,000244021
AA'	19	2	1	0,000239808
JJ'	16	3	2	0,000231107
CC'	23	7	1	0,000166583
EE'	24	8	2	0,000146028
II'	33	1	7	0,000110951
DD'	35	5	2	0,000124177
FF'	34	5	3	0,000120120
BB'	35	5	3	0,000117689
HH'	33	6	3	0,000119303

Network 4 (p=0,51)

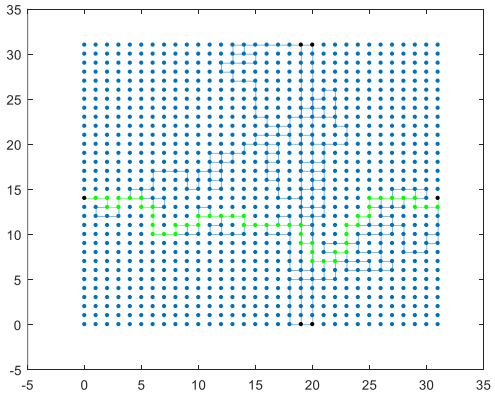

$$C = 0.0372\mathcal{H}^{-1}$$

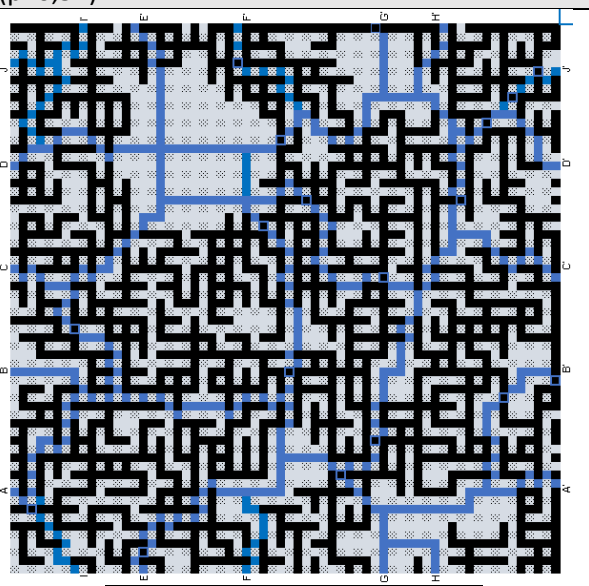

Res	172	229	444	
DD'	25	1	2	0,00018460
CC'	28	4	4	0,00013319
BB'	41	2	2	0,00011908
AA'	40	1	4	0,00011255
FF'	31	5	3	0,00012806
EE'	29	6	3	0,00012997

GG'	30	8	1	0,00013448
HH'	28	8	4	0,00011871
II'	50	5	2	0,00009405
JJ'	58	1	4	0,00008347

Network 5 (p=0,52)

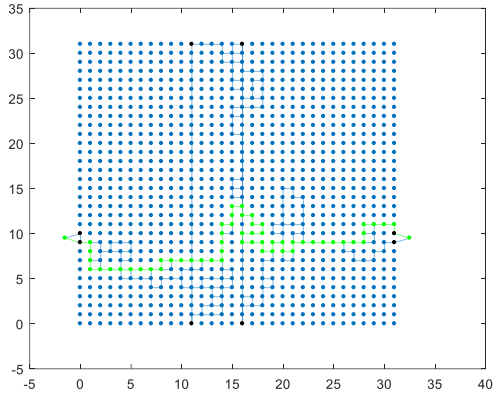

$$C = 0.0307\mathcal{H}^{-1}$$

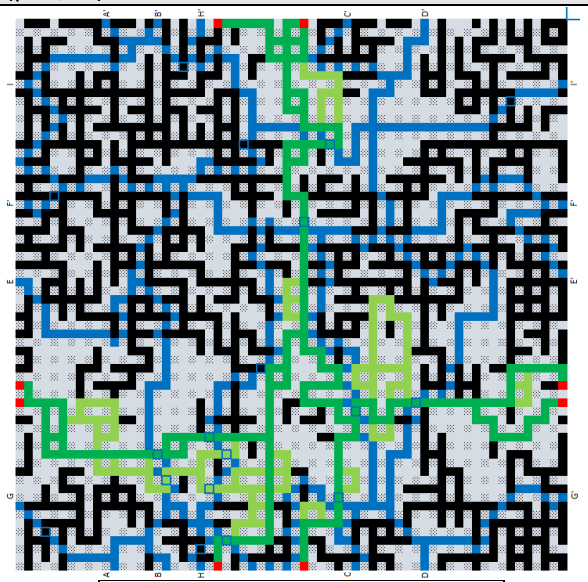

	R1	R2	Rb	C
Res	172	229	444	
DD'	26	2	1	0,00018608
II'	25	2	3	0,00016420
FF'	32	4	2	0,00013684
EE'	43	4	1	0,00011421
CC'	38	6	1	0,00011970
GG'	37	5	3	0,00011311
BB'	45	4	2	0,00010478
AA'	46	4	2	0,00010292
HH'	43	5	6	0,00008925

Network 6 (p=0,52)

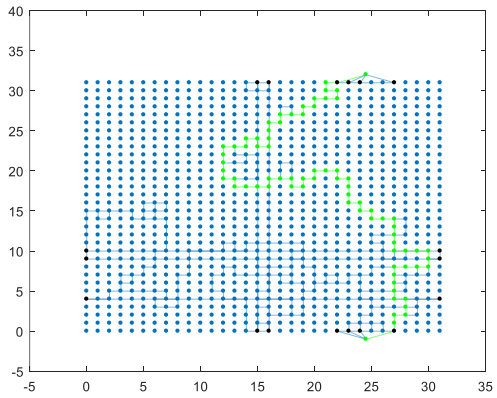

$$C = 0.0159\mathcal{H}^{-1}$$

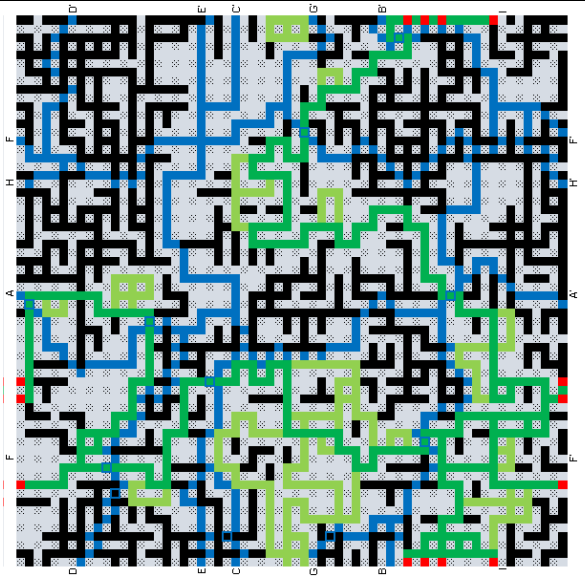

	R1	R2	Rb	C
Res	172	229	444	
CC'	15	1	2	0,00027049
EE'	19	1	1	0,00025374
FF'	36	2	1	0,00014096
AA'	30	3	3	0,00013930
DD'	42	2	2	0,00011669
HH'	39	4	1	0,00012395
BB'	35	6	3	0,00011460
GG'	48	4	4	0,00009134

Network 7 (p=0,51)

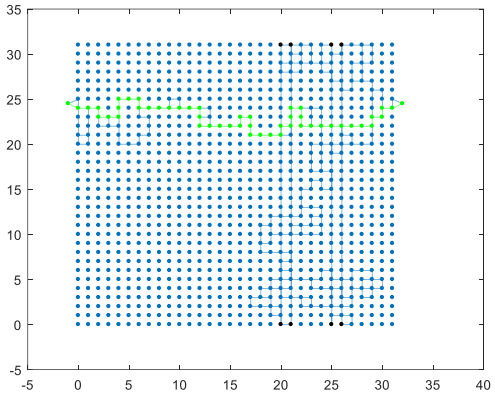

$$C = 0.0263\mathcal{H}^{-1}$$

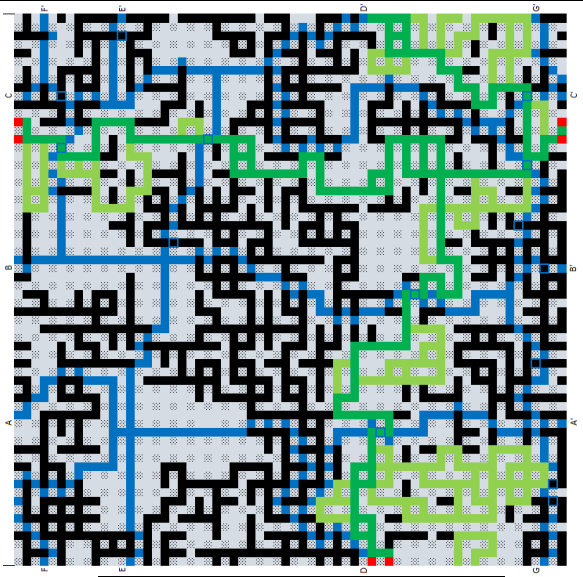

	R1	R2	Rb	C
Res	172	229	444	
AA'	32	5	1	0,00014098
BB'	29	2	2	0,00015788
CC'	32	6	2	0,00012877
DD'	44	4	2	0,00010670
EE'	24	2	3	0,00016898
FF'	28	4	2	0,00015106
GG'	46	5	6	0,00008532

Network 8 (p=0,48)

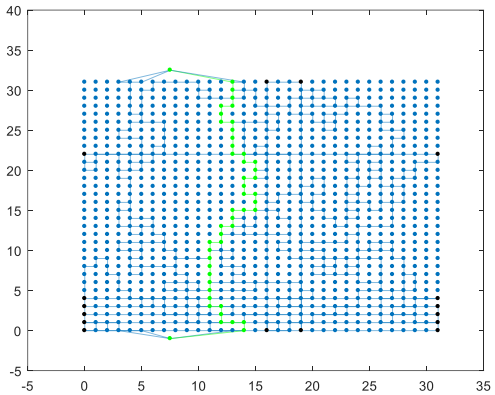

$$C = 0.0864\mathcal{H}^{-1}$$

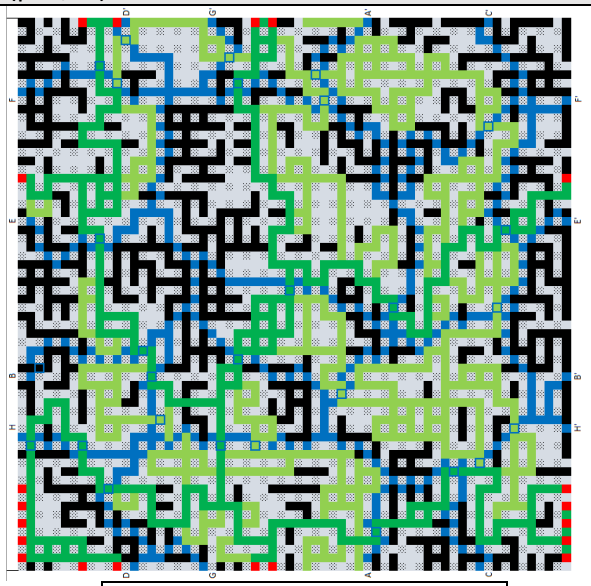

	R1	R2	Rb	C
Res	172	229	444	
DD'	32	5	4	0,00011869
EE'	42	6	3	0,00010070
GG'	40	5	5	0,00009761
HH'	38	5	6	0,00009667
CC'	43	6	4	0,00009482
AA'	49	5	4	0,00008811
FF'	53	3	5	0,00008317
BB'	42	8	5	0,00008868

Network 9 (p=0,47)

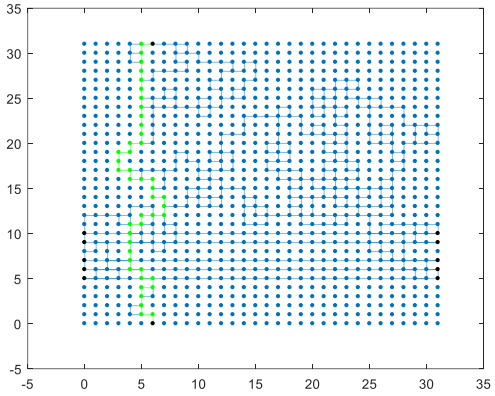

$$C = 0.0325\mathcal{H}^{-1}$$

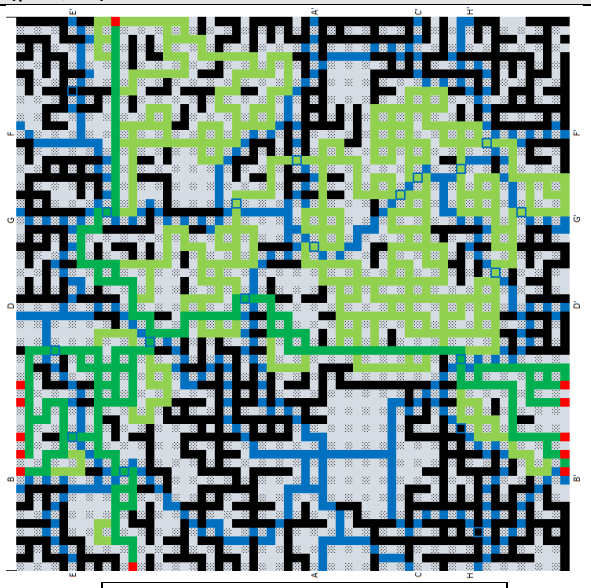

	R1	R2	Rb	C
Res	172	229	444	
BB'	35	4	2	0,00012781
AA'	32	6	2	0,00012877
EE'	44	3	3	0,00010431
DD'	36	7	2	0,00011517

CC'	37	7	2	0,00011293
FF'	41	11	1	0,00009985
GG'	36	8	7	0,00008983
HH'	53	7	5	0,00007729

Network 10 (p=0,45)

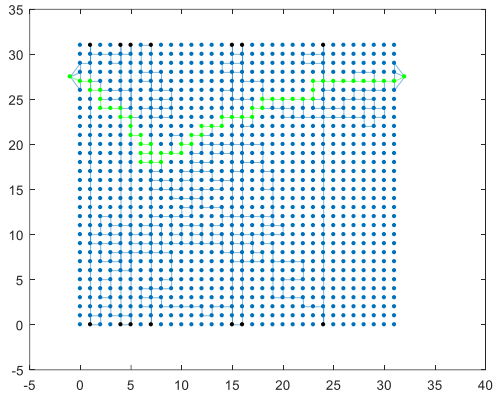

$$C = 0.0562\mathcal{H}^{-1}$$

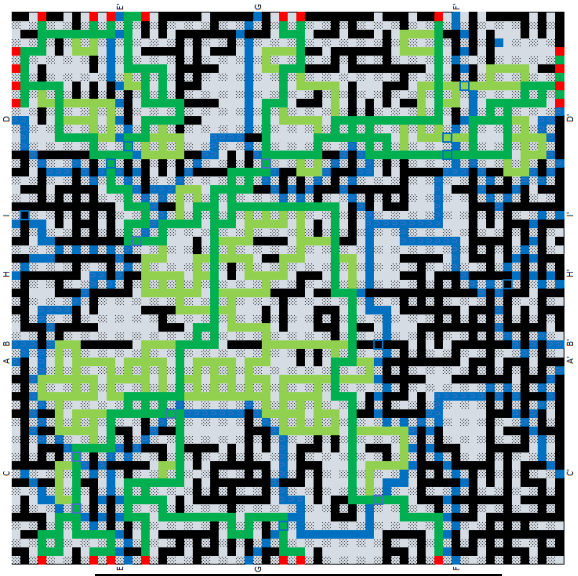

	R1	R2	Rb	C
Res	172	229	444	
CC'	38	5	3	0,00011095
DD'	56	1	2	0,00009303
FF'	35	7	4	0,00010639
BB'	55	3	2	0,00009062
AA'	47	5	3	0,00009469
GG'	45	5	4	0,00009380
HH'	50	5	3	0,00009028
II'	51	5	4	0,00008552
EE'	43	9	3	0,00009269

Network 11 (p=0,46)

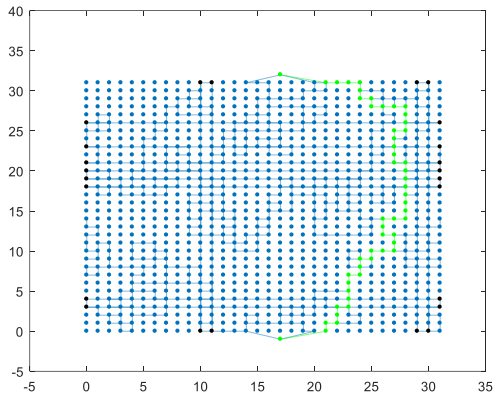

$$C = 0.0661\mathcal{H}^{-1}$$

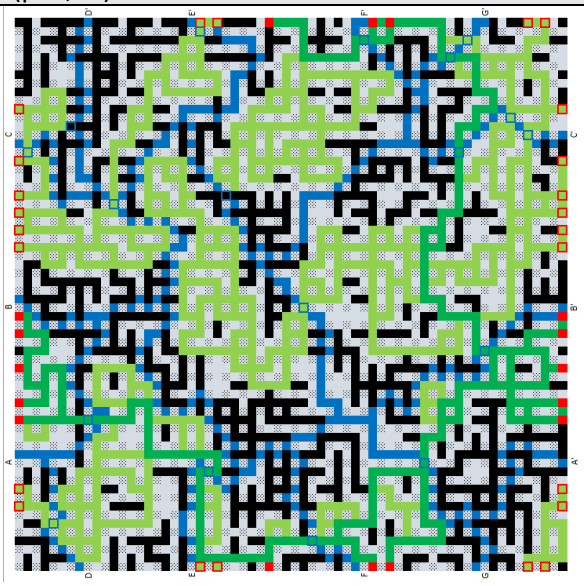

	R1	R2	Rb	C
Res	172	229	444	
FF'	43	2	3	0,00010886
GG'	40	3	4	0,00010703
DD'	51	6	4	0,00008388
BB'	54	8	2	0,00008328
EE'	49	11	2	0,00008450
CC'	56	7	6	0,00007195
AA'	55	11	2	0,00007772

Network 12 (p=0,54)

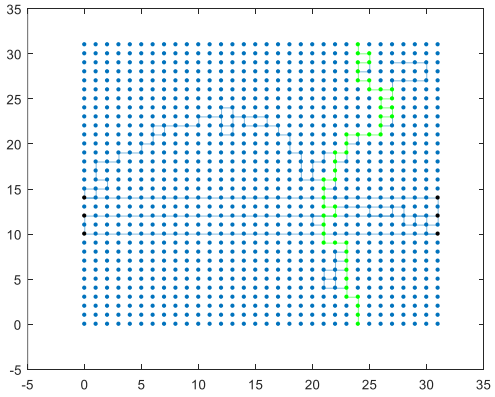

$$C = 0.0244\mathcal{H}^{-1}$$

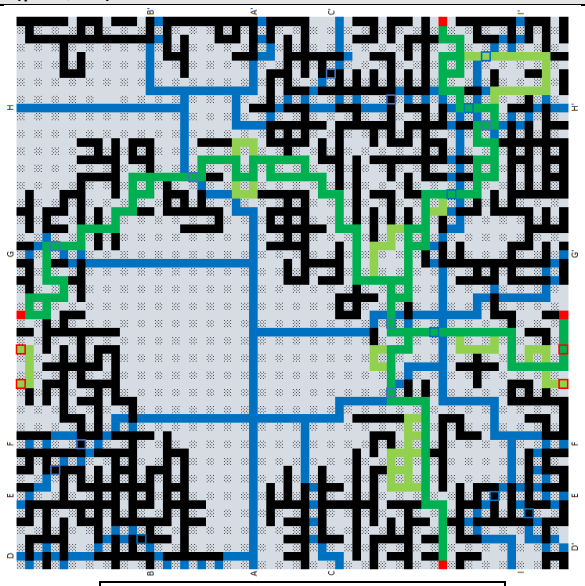

	R1	R2	Rb	C
Res	172	229	444	
AA'	7	1	1	0,00053277
BB'	7	4	1	0,00039002
GG'	18	1	2	0,00023736
FF'	12	3	2	0,00027480
EE'	21	2	2	0,00020169
CC'	15	4	2	0,00022810
HH'	22	4	2	0,00017895
DD'	28	4	3	0,00014156
II'	29	2	5	0,00013045

B3. MATLAB: Network graphs

This function creates two lists containing the begin (s) and end (t) nodes of the graph from the array in Excel. The script is a highly adapted version of Holstvoogd's (2020) script for percolation statistics.

Function: [S,T] = Jorijn(A,L)

A = Excel array of the gas backbone

L = Size, in this case L is 16 or 32.

After computing vectors s and t, they are used in the graph function of MATLAB to produce graph G.

Function: G = graph(S(1:2:end),T(1:2:end),ones(size(T(1:2:end))));

```
function [S T]=jorijn(A,L)
PS=L*(L/4);%total number of nodes

No=length(nonzeros(A(A>0))); %number of pore throats in the the lattice with bond
probility greater than 0
Lno=No*2;

S1=zeros(1,Lno); %inner nodes top to bottom
T1=zeros(1,Lno);

S2=zeros(1,Lno); %inner nodes left to right
T2=zeros(1,Lno);

S3=zeros(1,Lno); %top boundary
T3=zeros(1,Lno);

S4=zeros(1,Lno); %left boundary
T4=zeros(1,Lno);

%something to do with the pore bodies
for i=2:2:L
    for j=2:2:L
        A(i,j)=(j/2)+((i-2)/2)*(L/2);
    end
end

%inner nodes top-bot
for k=(3:2:L-1)
    for l=(2:2:L)
        m1=(k+l-4)+((k-3)/2)*L;
        m2=(k+l-3)+((k-3)/2)*L;
        if A(k,l)>0
            S1(1,m1)=A(k-1,l);
            S1(1,m2)=A(k+1,l);
            T1(1,m1)=A(k+1,l);
```

```
            T1(1,m2)=A(k-1,l);
        end
    end
end
S1( :, ~any(S1,1) ) = [];
T1( :, ~any(T1,1) ) = [];
%inner nodes left-right
for m=(2:2:L)
    for n=(3:2:L-1)
        m3=(m+n-4)+((m-2)/2)*L;
        m4=(m+n-3)+((m-2)/2)*L;
        if A(m,n)>0
            S2(1,m3)=A(m,n-1);
            S2(1,m4)=A(m,n+1);
            T2(1,m3)=A(m,n+1);
            T2(1,m4)=A(m,n-1);
        end
    end
end
S2( :, ~any(S2,1) ) = [];
T2( :, ~any(T2,1) ) = [];
%Top boundary conditions
for q=(2:2:L)
    m5=q-1;
    m6=q;
    if A(1,q)>0
        S3(1,m5)=A(2,q);
        S3(1,m6)=A(L,q);
        T3(1,m5)=A(L,q);
        T3(1,m6)=A(2,q);
    end
end
S3( :, ~any(S3,1) ) = [];
T3( :, ~any(T3,1) ) = []; %Left boundary conditions
for r=(2:2:L)
    m7=r-1;
    m8=r;
    if A(r,1)>0
        S4(1,m7)=A(r,2);
        S4(1,m8)=A(r,L);
        T4(1,m7)=A(r,L);
        T4(1,m8)=A(r,2);
    end
end
S4( :, ~any(S4,1) ) = [];
T4( :, ~any(T4,1) ) = [];

S=[S1,S2];%inner nodes
T=[T1,T2];
SLR=[S1,S2,S3];%segments left to right
TLR=[T1,T2,T3];
```

```
STB=[S1,S2,S4];%segments top to bottom
TTB=[T1,T2,T4];

% System Coordinates & Nodes

NoNodes = 1:PS;
[x,y] = meshgrid(0:1:((L/2)-1),0:1:((L/2)-1));
X=reshape(x,[],1);
Y=reshape(y,[],1);
nodes = [NoNodes;X' ;Y']';
segments = [(1:numel(S)) ; S ; T]';
segmentsLR = [(1:numel(SLR)) ; SLR ; TLR]'; %segments from left to right
segmentsTB = [(1:numel(STB)) ; STB ; TTB]';
end
```

B4. MATLAB: Node Elimination

The NODE function calculates the resistivity and conductivity of the network graph, G, between nodes a and b.

Function: [Res, Con] = NODE(G,X,Y,a,b,ext,order)

INPUT:

G = Network Graph

X,Y = coordinate system for the nodes

a,b = nodes (node number) between which the resistance is calculated

ext = vector of any external nodes that you do not want eliminated. Usually contains just a and b

order = vector of the node elimination order containing the degree of the to be eliminated nodes.

OUTPUT:

Res = equivalent resistivity between nodes a and b

Con = equivalent conductivity between nodes a and b

```
function [Res Con]=NODE(G,X,Y,a,b,ext,order)
% G = graph
% X,Y = coordinate system for the nodes
% a,b = nodes (node number) between which the two-point resistance is calculated
% ext = vector of external nodes that you do not want gone, usually ext=[a,b]
% order = vector of degrees, dictates the order in which nodes are
% eliminated

deg=order;
```

```
C=G;
figure;
% figure of plot beore node elimination comences
% after the first iteration you would prefer to put this off
h = plot(C,'EdgeLabel',C.Edges.Weight,'XData',X,'YData',Y);
P = shortestpath(C,a,b);
highlight(h,P,'NodeColor','g','EdgeColor','g')

for j=1:length(deg)
      clear L d
      L=laplacian(C);
      d=find(degree(C,1:numnodes(C))==deg(j));
      for k=1:length(ext)
      d=d(find(d~=ext(k)));
      end
    for i=1:length(d)
        n=d(i);
            degree(C,n);
            N = neighbors(C,n);
            c = findedge(C,N,ones(size(N))*n);
            cc = C.Edges.Weight(c);
            C = rmedge(C,N,ones(size(N))*n);
            A=ones(numel(N))-diag(ones(1,numel(N)));
            g=graph(A);
            tt=g.Edges;
            aa=table2array(tt);
            s=aa(:,1);
            t=aa(:,2);
            for nn=1:length(s)
                r = (cc(s(nn))*cc(t(nn))) / sum(cc);
                if findedge(C,N(s(nn)),N(t(nn)))==0
                    C=addedge(C,N(s(nn)),N(t(nn)),r);
                else
                    z = findedge(C,N(s(nn)),N(t(nn)));
                    C.Edges.Weight(z)=C.Edges.Weight(z)+r;
                end
            end
   end
figure; %figure of graph after elimination
h=plot(C,'EdgeLabel',C.Edges.Weight,'XData',X,'YData',Y);
P = shortestpath(C,a,b);
title(['Degree = ',num2str(deg(j))])
highlight(h,d,'NodeColor','r'); %highlight of eliminated nodes
highlight(h,P,'NodeColor','g','EdgeColor','g'); %highlight of shortest path

bbb=degree(C,1:numnodes(C));
bbb=bbb(find(bbb>1));
end
C.Edges %list of edges [begin|end|value)
L=laplacian(C);
    diag(L) %list of all the degrees within the graph
```

```
    deg=mode(bbb') %most common degree
numedges(C); %number of edges
Con=C.Edges.Weight;
Res=1/Con;
end
```

B5. MATLAB: Kirchhoff's solution

Function that implements Kirchhoff's solution to find the equivalent resistance between nodes ***a*** and ***b***. To use this function properly one has to run it twice. The first time is to see the graph of the network containing only connected nodes. This is necessary because the method does not allow non-zero rows or columns within the conductance matrix so unconnected nodes are removed. Therefore, the node numbers change because it is technically a new graph. The node numbers of the target nodes are read from the new graph (use the data tip tool) and inputted as ***a*** and ***b*** in the second run of the script.

Function: [R,C] = Kirchhoff(G1,X,Y,ab,b)

INPUT:

G1 = Network Graph

X,Y = coordinate system for the nodes

a,b = nodes (node number) between which the resistance is calculated

OUTPUT:

R = equivalent resistivity between nodes a and b

C = equivalent conductivity between nodes a and b

```
function [R C] = Kirchhoff(G1,X,Y,ab,b)
La=laplacian(G1);
C=rmnode(G1,find(diag(La)==0));
figure; plot(C,'XData',X(find(diag(La)>0)),'YData',Y(find(diag(La)>0)));

LA=laplacian(C);
LA=full(LA);

if sum(LA,1)~=0 | sum(LA,2)~=0 | isempty(find(diag(LA)==0))==0
   sprintf('WRONG')
end

g1=LA([ab],[ab]);
g2=LA([b],[b]);
R = det(g1)/det(g2);
C = 1/R;
end
```